Segmentation of endothelial cells of the cornea from the distance map of confocal microscope images

Raidel Herrera-Pereda, Alberto Taboada Crispi, Danilo Babin, Wilfried Philips

PII: S0010-4825(21)00747-2

DOI: https://doi.org/10.1016/j.compbiomed.2021.104953

Reference: CBM 104953

To appear in: *Computers in Biology and Medicine*

Received Date: 27 June 2021

Revised Date: 14 October 2021

Accepted Date: 15 October 2021

Please cite this article as: R. Herrera-Pereda, A.T. Crispi, D. Babin, W. Philips, Segmentation of endothelial cells of the cornea from the distance map of confocal microscope images, *Computers in Biology and Medicine* (2021), doi: https://doi.org/10.1016/j.compbiomed.2021.104953.

Segmentation of endothelial cells of the cornea from the distance map of confocal microscope images

Raidel Herrera-Pereda, Alberto Taboada Crispi, Danilo Babin, Wilfried Philips

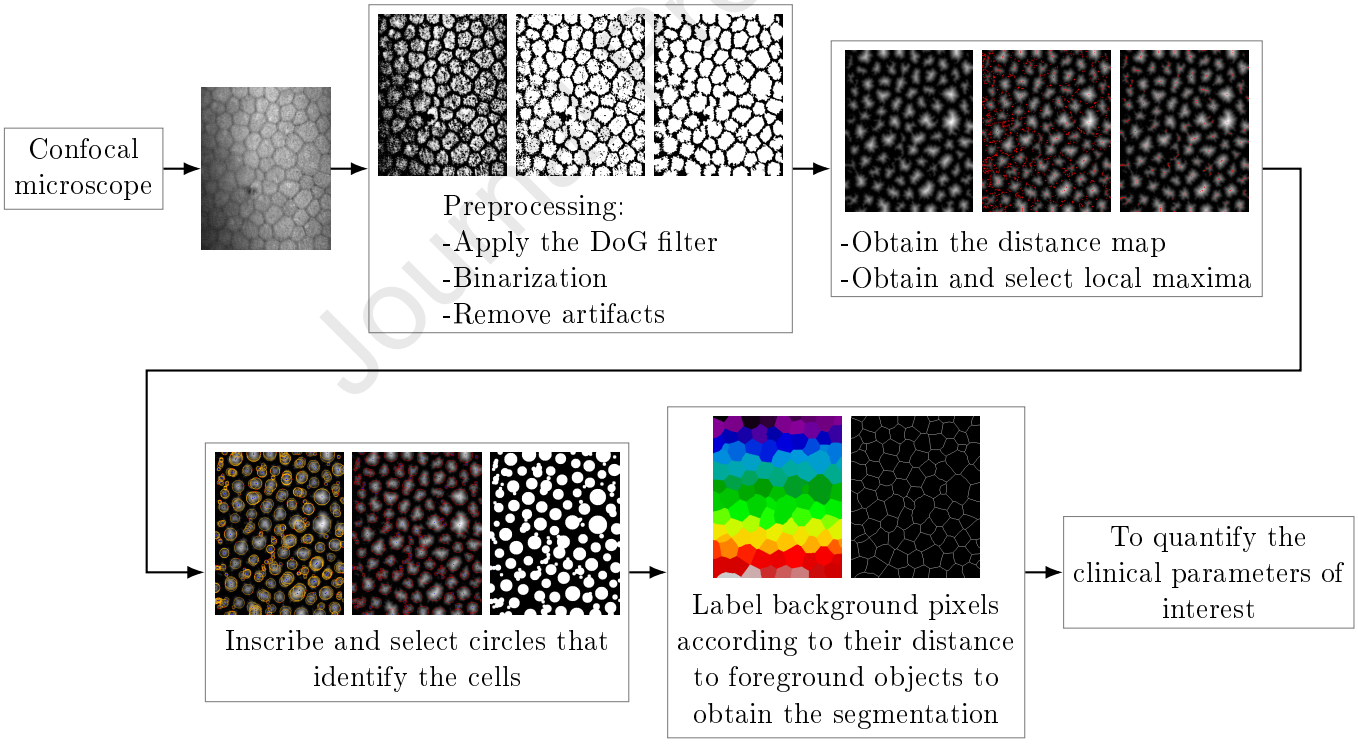

Graphical Abstract

Segmentation of endothelial cells of the cornea from the distance map of confocal microscope images

Raidel Herrera-Pereda, Alberto Taboada Crispi, Danilo Babin, Wilfried Philips

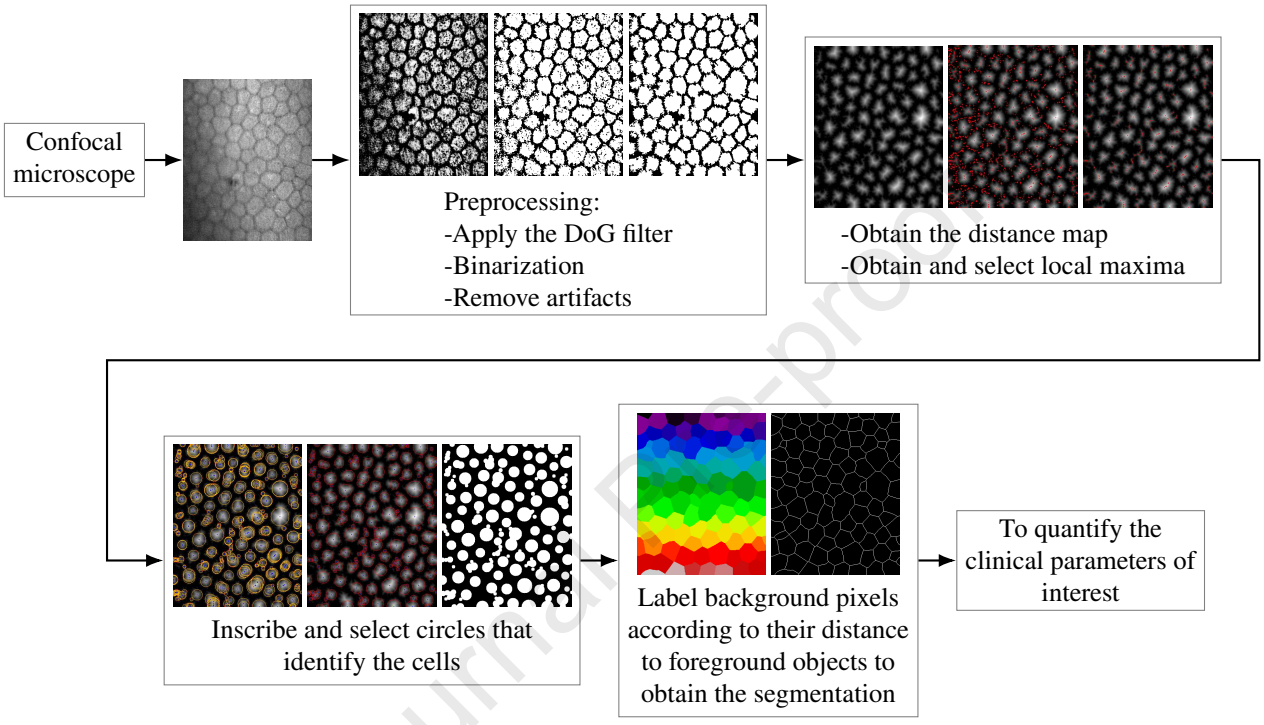

Highlights

Segmentation of endothelial cells of the cornea from the distance map of confocal microscope images

Raidel Herrera-Pereda, Alberto Taboada Crispi, Danilo Babin, Wilfried Philips

- A difference of Gaussian is applied to enhance cell borders and to obtain the inter-cellular space with minimal value, which we then used as a threshold for obtaining a binary image.
- A frequency-domain analysis allows obtaining a global adaptive threshold value per image for automatically removing artifacts in the binary images.
- Local maxima, selected in the distance map of the binary image, are used as centers of circles inscribed in the cells. A selection of the inscribed circles is intended to detect individual cells, aiming also to separate those cells that appear merged in the image.
- The segmentation of the cell's contours is achieved simply by labeling each background pixel according to its distance to the nearest foreground object.
- Quantification and comparison with ground truth and two methods are achieved for measuring clinical parameters of interest and assessing the results, including cell count, cell density, polymegathism, and pleomorphism. Results outperform those from one of the methods in all quantified parameters and surpass another method in estimated polymegathism.

Segmentation of endothelial cells of the cornea from the distance map of confocal microscope images⋆

Raidel Herrera-Pereda[a,c,*], Alberto Taboada Crispi[b], Danilo Babin[c] and Wilfried Philips[c]

[a]Departamento de Bioinformática, Facultad de Ciencias y Tecnologías Computacionales, Universidad de las Ciencias Informáticas (UCI), Carretera a San Antonio de los Baños Km 2 ½, Torrens, Boyeros, La Habana, Cuba.

[b]Centro de Investigaciones de la Informática, Universidad Central "Marta Abreu" de Las Villas (UCLV), Carretera a Camajuaní, km 5 ½, Santa Clara, VC, CP 54830, Cuba.

[c]TELIN-IPI, Ghent University - imec, Belgium.

ARTICLE INFO

Keywords:
corneal endothelial cells
confocal microscopy images
image frequency spectrum
distance map
segmentation

ABSTRACT

We propose a novel algorithm for segmenting cells of the cornea endothelium layer on confocal microscope images. To get an inter-cellular space with minimum gray-scale value and to enhance cell borders, we apply a difference of Gaussian filter before image binarization by thresholding with the minimum gray-scale value. Removal of segmented noise and artifacts is performed by automatic thresholding (using an image frequency analysis to obtain a global threshold value per image). Final segmentation of cells is achieved by fitting the largest inscribed circles into the centers of cell regions defined by the distance map of the binary images. Parameters of interest such as cell count and density, pleomorphism, polymegathism, and F-measure are computed on a publicly available data-set (Confocal Corneal Endothelial Microscopy Data Set - Rotterdam Ophthalmic Data Repository) and compared against the results of the segmentation methods included with the data set, and the results of state of the art automatic methods. The obtained results achieve higher accuracy compared to the results of the segmentation included with the data set (e.g., -proposed versus dataset in R^2 and mean relative error-, cell count: 0.823, −0.241 versus 0.017, 0.534; cell density: 0.933, −0.067 versus 0.154, 0.639; cell polymegathism: 0.652, −0.079 versus 0.075, 0.886; cell pleomorphism: 0.242, −0.128 versus 0.0352, −0.222, respectively), and are in good agreement with the results of the state of the art method.

1. Introduction

In-vivo confocal microscopy (IVCM) is an important diagnostic tool through which it is possible to obtain images in a non-invasive way, allowing the analysis of corneal structures in the living eye. The corneal endothelium forms a single layer of cells describing a shape with a hexagonal pattern on the posterior corneal surface. Clinically, it is functionally essential to the cornea. It has the basic function of maintaining corneal hydration and transparency [6]. Endothelial cells do not reproduce, thus, dead cells are replaced by the surrounding cells. Consequently, the total number of cells, their size, and regular structure are affected by age and pathologies [6, 24]. Therefore, morphometric studies in the corneal endothelium provide clinical information that allows us to assess the cornea's health state [24].

Cell density is a very important parameter when assessing the condition of the corneal endothelium. It can be obtained directly through frequency analysis without having to produce the segmentation of cells [5, 21, 2, 3, 25]. Nevertheless, the segmentation of cells has been reported to yield an improved result of cell density compared to the estimates obtained through frequency analysis [25]. Another important argument in favor of segmentation is the possibility to quantify other parameters of interest, such as variation of cell size and shape [25, 24], which is not achievable using the frequency analysis approach. Segmentation-dependent measures rely on accurate and robust segmentation methods and, for this reason, are not yet as widely used in clinical practice as frequency analysis methods[25, 30]. The goal of our research is to design a robust endothelial cell segmentation method for the quantification of parameters of interest and to facilitate their application in clinical practice.

The automatic analysis of the human cornea endothelium in Confocal Microscopy (CM) images has been reported previously. The built-in software supplied by Tomey ConfoScan P4 slit-scanning microscope (Tomey, Erlangen - Tennenlohe, Germany) was used for automatic analysis in [13]. Two methods were applied in [25]: a frequency analysis aiming to obtain endothelial cell density and a segmentation method through stochastic watershed.

The authors in [26] proposed the following steps to automatically classify images according to the main layers of the cornea and to generate a 3D model: image classification (through Artificial Neural Networks (ANN), Adaptive Neuro-Fuzzy Inference Systems (ANFIS), and a combination of both), global adaptive thresholding, connected component labeling, and image registration using Speeded-Up Robust Features (SURF) and Scale Invariant Feature Transform (SIFT) approaches.

Two tracking procedures are applied in [18]: tracking of

⋆This work (or part of the work) was supported by the Special Research Fund (BOF) of Ghent University, Belgium, Grant Code 01W03516.

We thank to the Rotterdam Ophthalmic Institute, the Rotterdam Ophthalmic Data Repository (http://rod-rep.com) and Juan P. Vigueras-Guillén for their collaboration to dispel our doubts around the used data-set.

*Corresponding author

Raidel.HerreraPereda@UGent.be, rherrera@uci.cu (R. Herrera-Pereda)

ORCID(s): 0000-0003-0893-0926 (R. Herrera-Pereda)

valleys dividing the cells for extracting their contours, and a tracking procedure for tracing rays from elevated points. A further improvement procedure is achieved by adjusting the segmentation according to its lowest local values pixel neighbors (in case of its existence) in the original image.

In [9], the authors present a semi-automatic method for analyzing images of the corneal endothelium based on skeletonization and connected component analysis (on the obtained skeleton). A classification of the connected components as cells is obtained using predetermined threshold values of area, perimeter, and length.

A fully automatic segmentation algorithm based on Feed-Forward Artificial Neural Network (FF-ANN) is proposed in [4], whereas in [16], the automatic algorithm is based on K-means and watershed. Watershed and Voronoi Tessellation are used for segmentation in [1]. The authors in [23, 24] propose automatic cell segmentation methods based on genetic algorithm. In [27], a snake model in combination with particle swarm optimization is proposed to achieve an automatic endothelial cell segmentation. In [29], a support vector machine classifier (SVM) is applied to identify and merge superpixels constituting cells.

The aforementioned automatic methods still produce too many differences compared to human (manual) analysis. The differences relate to the dependence on selected features of the neural network training data-set in [4] (e.g., only well-defined borders are manually marked in the ground truth images used for training), the loss of image quality at the borders of the images in [1], and the differences (partly) in the measuring techniques in [13].

According to [14, 17], the endothelial cell contours obtained through IVCM built-in software may require manual corrections. In [13], cell count and cell density results of an automatic analysis through the built-in software supplied by the Tomey ConfoScan P4 slit-scanning microscope (Tomey, Erlangen-Tennenlohe, Germany) have statistically significant differences when compared to the manual measures. Moreover, automatic methods may produce errors in identifying endothelial cell contours ([15, 14, 17, 24]), yielding (for instance) to over-segmentation [19], which affects the cell density when compared to manual analysis [13, 17]. Thus, automatic results may require manual corrections of the inaccuracies [11, 17, 20, 24].

The image segmentation software used in clinical practice is often semi-automatic, which reduces the reproducibility and accuracy of quantified parameters. The acquired images are often affected by noise, artifacts, uneven illumination, and out-of-focus (blurred) areas, which cause segmentation problems. Thus, manual corrections often have to be made, making the complete analysis tedious, time-consuming, and impractical in the clinical setting [24, 4, 1]. Therefore, there is a clear need for a (semi-)automatic, easy-to-use, accurate, and robust method for endothelial cell segmentation in IVCM images of the human cornea. For a more complete review on digital image analysis for corneal images see [12].

In this work, we propose a novel method for segmenting human corneal endothelial cells from IVCM images. Our method enhances cell borders, deals with uneven illumination and contrast present in the images, and automatically removes artifacts in binary images. Artifact removal is achieved by automatic thresholding, where the threshold is determined by frequency analysis of the images. For cell segmentation, we propose a method based on fitting circular regions using a distance map generated on the filtered binary image. The convex polygonal shape of endothelial cells motivates to use inscribed circles as a mean to identify the cells, which we confirm. We also demonstrate that inscribed circles can be useful for separating erroneously merged cells that hinder the cell segmentation process.

The results section (i.e., section 3) shows graphs of cell count, density, polymegathism, pleomorphism, and F-measure, for visual comparison. It also shows QQ-plots for the graphical test of data normality, box-plots of relative errors, as well as quantitative normality test results, correlation coefficient values, and relative error statistics in tables. The Appendix (section 6) shows the results and associated errors comparing with the manual measures from all included methods.

2. Methods

The proposed method consists of two major steps. The first step (preprocessing) is used to enhance cell boundaries, deal with uneven illumination and contrast found in IVCM images, and remove artifacts. The second step deals with the actual segmentation of cells by fitting selected circles to a distance map calculated on the binary image of the preprocessing step.

2.1. Preprocessing

IVCM images of the endothelium layer of the cornea often have a non-uniform luminosity and contrast [22] (see Figure 1a). Frequently, these images are blurred, distorted, and contain noise due to the anatomy of the cornea and the characteristics of the image acquisition process [26, 24, 10, 1]. Therefore, preprocessing the images to improve their quality (removing noise, artifacts, and blur) is an important step that can highly influence the quality of the segmentation.

2.1.1. Edge enhancement and inter-cellular space definition

To enhance the borders of cells and obtain an inter-cellular space with minimum value are the first goals of the preprocessing in this work because it helps in the subsequent cell delineation. For this purpose, we use a Difference of Gaussian filter (DoG filter, [28] page 142) as an approximation of the Laplacian of Gaussian (LoG) edge detector filter, which reduces the noise susceptibility of the Laplacian operator:

$$\Gamma_{\sigma_1,\sigma_2}(x,y) = \frac{e^{-\frac{x^2+y^2}{2\sigma_1^2}}}{\pi\sigma_1^2} - \frac{e^{-\frac{x^2+y^2}{2\sigma_2^2}}}{\pi\sigma_2^2} \tag{1}$$

The DoG filter consists of taking the difference of two differently sized Gaussians (values σ_1 and σ_2, see Equation 1).

The resulting image from the applied DoG filtering (i.e., $DoG(x, y)$) has the characteristic of having the inter-cellular space (hereafter image background) with the minimum gray scale intensity found in the image (see Figure 1b). Our experiments show that the implementation of the DoG filter in OpenCV for C/C++ programming language, with first and second kernel sizes of [3x3] and [103x103] respectively (empirically determined using the GaussianBlur function), generates the desired DoG-filtered image. The GaussianBlur function computes the σ values from the kernel sizes (see OpenCV documentation).

2.1.2. *Image binarization and artifact removal*

After applying the DoG filter (see subsection subsubsection 2.1.1 and Figure 1b), we perform an initial segmentation by thresholding with the minimum gray scale value in the preprocessed image (i.e., we label as foreground pixel every pixel with value different than the minimum gray scale value, see Figure 1c and algorithm 1).

Algorithm 1: Image binarization

```
Input: DoG(x,y) ;          // (i.e., DoG filtered image)
Output: BW(x,y) ;          // (i.e., Binary image)
if DoG(x,y) > min{DoG(x,y)} then
    DoG(x,y) = 255 ;       // (i.e., foreground)
else
    DoG(x,y) = 0 ;         // (i.e., background)
```

The resulting images contain artifacts smaller than the cell area, manifesting as background pixels in the area of the cell body (holes) and foreground pixels in the area between the cells, as seen in Figure 1c, Figure 2a, and Figure 2b. Since the artifacts manifest as regions with significantly smaller area compared to cell size, we use connected component analysis to compute the area of each region and apply thresholding by area. We apply, as threshold value T, a scaled version of the average cell area intending to only remove artifacts from the image.

For determining the average cell area, counting the number of pixels in each connected component and finding the average could produce a larger value than the actual average cell area because cells may appear connected in the initial segmentation image. Therefore, we apply a fully automatic method in the frequency domain. It consists of obtaining the two-dimensional representation in the frequency domain of the image by applying the 2D Fast Fourier Transform (2DFFT, see Figure 3b). Then, we use a 1D orientation invariant representation [25] (see Figure 3d) to compute the radial mean of the frequency content's magnitude in polar form (see Figure 3c and 3d):

$$F_{RM}(f) = \frac{1}{2\pi}\int_0^{2\pi} \mid F(f,\theta) \mid \, d\theta \qquad (2)$$

In Equation 2, $F(f,\theta)$ is the polar frequency spectrum corresponding to the Fourier transform of the image. For

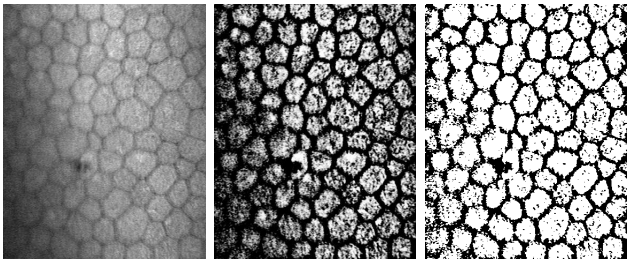

(a) (b) (c)

Figure 1: DoG filtering and binarization of a human corneal endothelium image. (a) Original confocal microscope image of endothelial cell layer. Representative of the used dataset [25]. (b) Result of DoG filtering (i.e., DoG(x,y) image) and histogram equalizing the image in (a). The histogram equalization responds to a better visualization (in this figure) only. (c) Result of the binarization of DoG(x,y) (i.e., BW(x,y) image) (subsubsection 2.1.2).

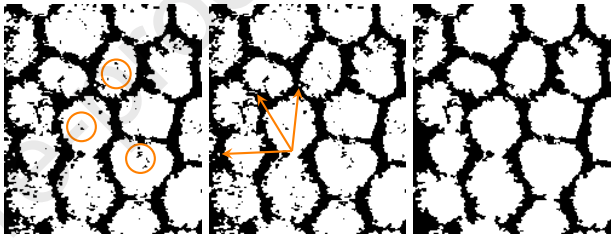

(a) (b) (c)

Figure 2: Example of artifacts on the binary image. (a) Holes in cell body (enclosed by circles), (b) Foreground artifacts in inter-cellular space (pointed by arrows), (c) Result of removing holes and foreground artifacts.

computing the radial mean the output is sampled at frequencies $f = \{0, \frac{1}{N}, \frac{2}{N}, ..., \frac{1}{2}\}\ pixel^{-1}$ [25]. We select N to be the smallest side of the image in pixels and assuming in this step a square image of NxN pixels. Also, we use N/2 as the radius of the circle that bounds the area to be transformed to polar form.

The radial-mean function $F_{RM}(f)$ includes two largest peaks, one at $f = 0$ (i.e., zero frequency) related to the slow variation in pixels intensity and the other one at the frequency of the repetitive cell pattern (i.e., the characteristic frequency f^*) [21]. In some images, the peak of $\mid F(f,\theta) \mid$ at $f = 0$ may decay very slowly, making difficult to detect the peak at f^*, and consequently making hard to detect f^* [25]. Thus, for enhancing the peak at f^* (as in [25]), we apply a dilation by reconstruction (see also "Morphological Reconstruction" in [8]) of the pixel at $f = 0$ with $\mid F \mid$ as mask, until stability is reached. We use the origin pixel and its 4-neighborhood as the structuring element of the dilation operation. The result of this procedure can be seen in Figure 3b.

Different methods have been used for obtaining the characteristic frequency f^* from the radial mean function [5, 21, 3, 25]. We take in this study, like in [3], the position of the first (largest) peak (after removing the one at $f = 0$) in the

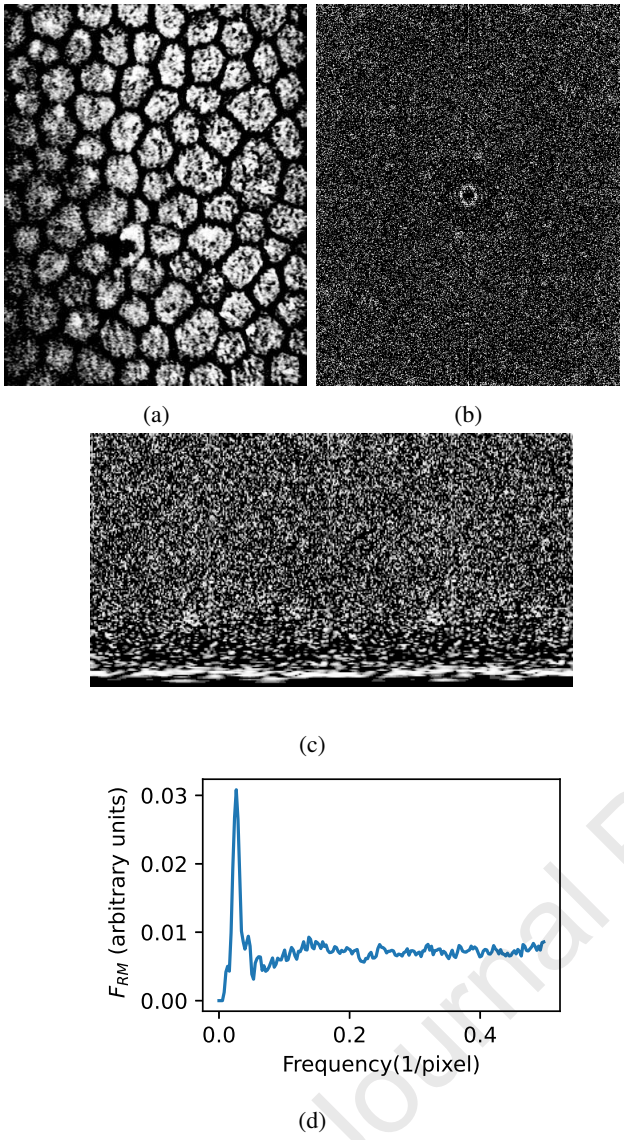

Figure 3: (a) DoG filtered image with histogram equalization, (b) 2DFFT of (a) with central ring enhancement and without the local maximum at $f = 0$, (c) Polar form of (b), and (d) Radial mean from (c). Images (b) and (c) are histogram-equalized for visualization purpose in this figure only.

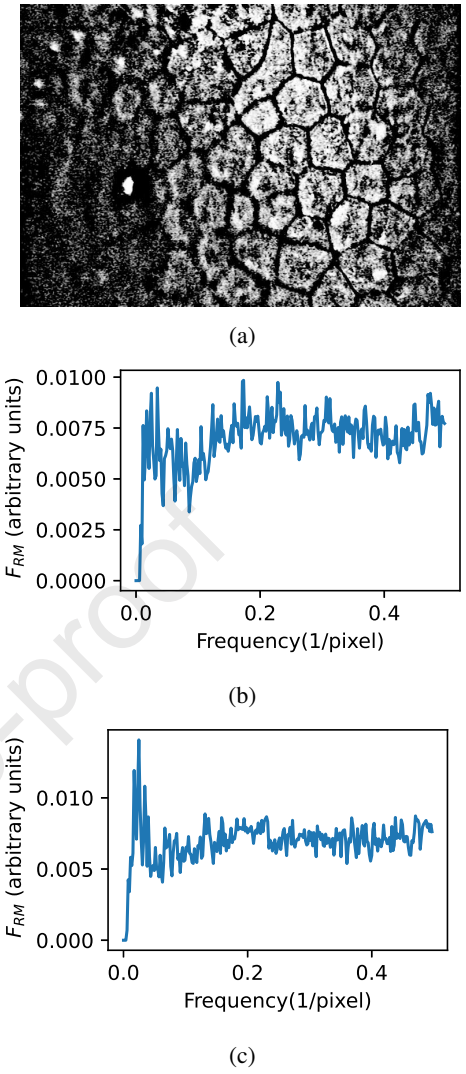

Figure 4: Influence of the image histogram equalization in the radial mean function. (a) DoG filtered and histogram-equalized image. (b) The radial mean obtained from the frequency analysis (see subsubsection 2.1.2) of the DoG filtered image (without histogram equalization) showing a not easy recognizable central ring radius peak. (c) The radial mean obtained from the frequency analysis of (a), where the central ring radius at f^* is clearly recognizable (the largest peak).

$F_{RM}(f)$ function as the characteristic frequency f^* (see Figure 3d).

Before obtaining the Fourier transform, we apply histogram equalization to the $DoG(x, y)$ image (see Figure 3a, Figure 4a) to enhance its contrast. The histogram equalization step generates an enhanced central ring in the resulting spectrum image, and consequently in the radial mean function, see Figure 4c. Otherwise, the peak at f^* may not be recognizable in the radial mean function, see Figure 4b.

The cell average area per image (A_{avg}) can then be computed using the characteristic frequency [25],

$$A_{avg} = \alpha L^2 = \frac{\alpha}{f^{*2}} \tag{3}$$

In Equation 3, α is a parameter dependent on the shape and regularity of the cells, and L the most common cell width [25]. In this work, we set the α value to 1 [5, 21, 2, 3, 25].

We compute two threshold values T_1 and T_2 based on A_{avg} and the central ring pattern of the frequency spectrum. The central ring pattern is observed in the frequency spectrum of the image due to the approximately hexagonal shape of the endothelial cells [5] (see Figure 3b). The ring radius r is inversely proportional to cells' size. Thus, a smaller cell structure produces a larger ring in the image frequency spectrum than a larger cell structure. Therefore, we use the numerical value of the ring radius at the characteristic frequency of the image (i.e., defined as n_{rf^*}, with no dimension

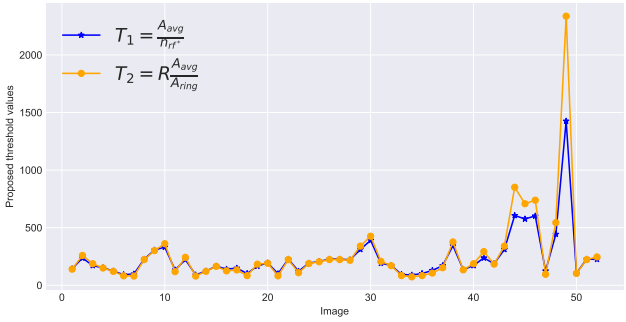

Figure 5: Threshold values sample plots.

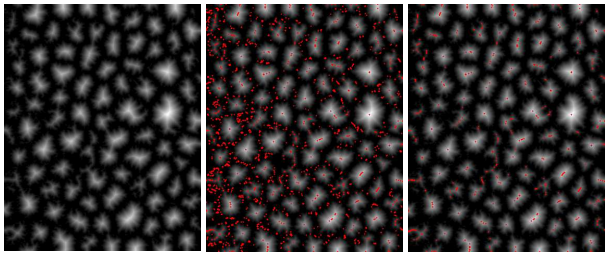

(a) (b) (c)

Figure 6: The distance map image and peaks (marked with red dots): (a) distance map, (b) all peaks (marked with red dots), (c) selected peaks (marked with red dots) by thresholding.

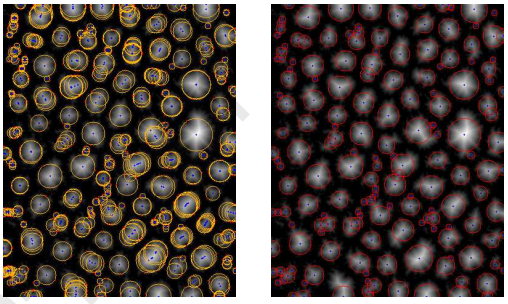

(a) (b)

Figure 7: Circles that were fitted into the inner body of the cells. (a) total number of found circles, (b) selected circles.

assigned) as a scaling down factor of the mean cell area A_{avg} for computing the threshold value T_1:

$$T_1 = \frac{A_{avg}}{n_{rf*}} \tag{4}$$

We also tested the second threshold value T_2 as A_{avg} divided by the area of the ring at f^* in the frequency image. In this case, the resulting threshold value is not useful because it is to small and a scaling-up coefficient should be used to approach the needed value (see Equation 5). We propose a coefficient value $R = 30.886$ (empirically found) that proved to produce similar results as threshold T_1. Sample plots of both threshold values are presented in Figure 5 for visual comparison.

$$T_2 = R\frac{A_{avg}}{A_{ring}} \tag{5}$$

The obtained thresholds applied to the used data set proved to be effective for artifact removal without affecting the smallest cells in the image. The smallest cells can be removed if the average area of the cell is directly used as a threshold for artifact removal. Hence, we divide by n_{rf*} or by A_{ring} although in the latter a multiplication by a scaling-up coefficient is needed. We refer to the used threshold values for artifact removal in our proposed method as "Proposed (Tx)", where x takes values 1 or 2. Figure 2c shows a sample image after removing its artifacts.

2.2. Cell segmentation

After filtering artifacts from the initial segmentation, the resulting image may still contain merged cells that hamper accurate cell segmentation (e.g., Figure 2c). We propose in this paper to exploit the polygonal shape of the corneal endothelial cells and perform cell separation by fitting circles to cell candidate regions. To find the best candidates for cell centers, we perform a distance transform on the initially segmented image. In the resulting distance map image, the value of each pixel represents the Euclidean distance to the closest background pixel. Hence, the pixels in the center of the cells will be the brightest (locally) in the distance map image and could be used as centers of inscribed circles. The first step in our approach is to find local maxima (i.e., peaks) in the distance map image aiming to detect the centers of the cells. However, besides the actual cell centers, local maxima are also found in peripheral regions (see Figure 6b). Hence, we apply an empirically found threshold value of $L/8$ to remove the unwanted peaks pixels (i.e., peaks with pixel value lower than $L/8$ are removed, see Figure 6c).

Subsequently, we fit circles into the inner boundaries of the cells using the selected peaks as cell centers (see Figure 7a and Figure 8a). In case of multiple closely overlapping circles (due to their proximity, points eligible for the center of the cell, may fall inside another inscribed circle), we filter out the matched circles to leave only the one with the largest radius (see Figure 7b and Figure 8b).

Finally, we merge the remaining intersecting circles and create a binary image by labeling all pixels in the circles as foreground pixels (see Figure 9a). From the resulting binary image, a region segmentation is obtained by labeling each background pixel according to its proximity to the merged circles (see Figure 9b). A line segmentation can then be produced at the edges of different labels (see Figure 9c). A schematic representation of the proposed segmentation procedure can be seen in Figure 10.

3. Materials and Results

For evaluating our method, we use a data set that includes 52 confocal images of corneal endothelium publicly avail-

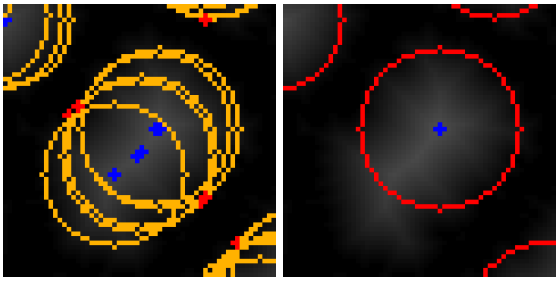

(a) (b)

Figure 8: Close-up of fitted circles. (a) circles fitted into a foreground object in the distance map image, (b) automatically selected circle in (a).

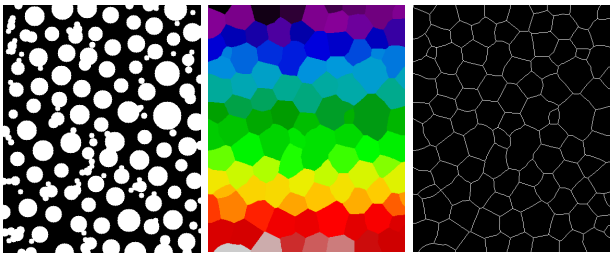

(a) (b) (c)

Figure 9: Segmentation obtained from the image with merged circles. (a) merged circles as foreground objects, (b) region segmentation obtained from (a), (c) one pixel wide line segmentation.

able from the Rotterdam Ophthalmic Data Repository [25]. The data set contains also (in separate segmented images) corresponding regions of interest for each image (see Figure 11b) and images with positions of cell centers (i.e., a point was placed approximately in the middle of each cell, see Figure 11c) made manually by an expert. Measures of cell count, density, pleomorphism, and polymegathism, obtained from manually assisted segmentation were also included. We compare our method to the measurements of endothelial parameters obtained by the software NAVIS (i.e., the Confoscan 4 microscope's software, Nidek Technologies Srl, Padova, Italy) and the automatic results from Selig et al. ([25]) and Vigueras-Guillén et al. ([29], kindly shared after request). The measured parameters are defined below.

- Cell count (N_c).
- Cell density ($\rho_c = \frac{N_c}{A_t}$, [24]), where A_t denotes the area of the total of cells.
- Polymegathism (CV: cell size variation coefficient) is computed as the ratio of standard deviation of cell area (σ_A) over the average cell area [24]:

$$CV = \frac{\sigma_A}{A_{avg}} 100\% \tag{6}$$

- Pleomorphism (i.e., HEX: cell shape variation coefficient or hexagonality) is the fraction of hexagonal cells (N_{chex}) over the total number of cells [24] (the number of cell's sides is computed in this work by counting the number of neighboring cells for each segmented cell):

$$HEX = \frac{N_{chex}}{N_c} 100\% \tag{7}$$

- F-measure [25] defined as

$$F = 2\frac{pr}{p+r} \tag{8}$$

with

$$p = \frac{n_{corr}}{n_{total}}, \qquad r = \frac{n_{corr}}{n_{eval}},$$

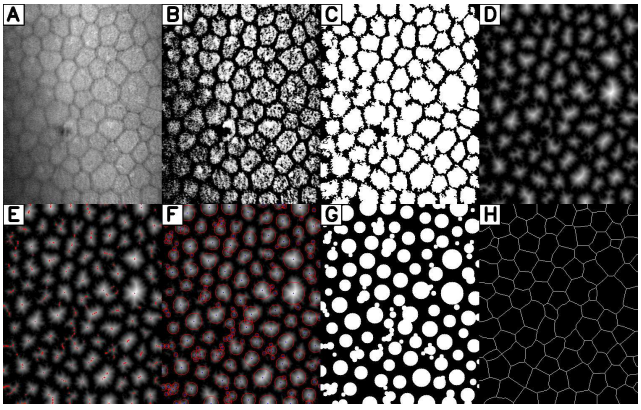

Figure 10: Schematic representation of the proposed segmentation process. (A) Original image. (B) DoG filtered image (histogram-equalized for visualization purpose only) (subsubsection 2.1.1). (C) The image in B is converted to binary by using a threshold value of minimum gray scale value. Subsequently, artifacts are removed by using a threshold value per image found through a frequency analysis of the image in B (subsubsection 2.1.2). (D) Distance map of the image in C, (E) Selected local maxima by an empirically found threshold, (F) Selected circles by an automatic custom method, (G) Merged circles (i.e., foreground objects) in image converted to binary, (H) Line segmentation (subsection 2.2).

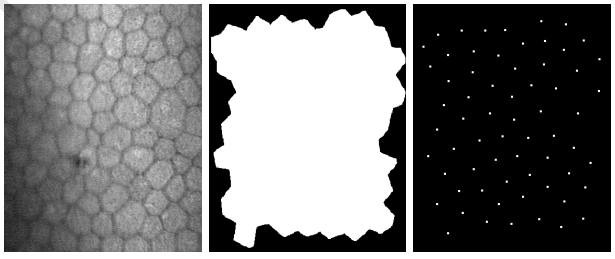

(a) (b) (c)

Figure 11: Representative images from the used dataset [25]: (a) original confocal microscope image of endothelial cell layer, (b) manually selected ROI corresponding to the original image in (a), (c) manually selected point-markers corresponding to the approximate cell centers inside the ROI from the image in (a). The points have been enlarged so they are better visible.

where n_{corr} is the number of correctly segmented regions, n_{total} is the total number of regions and n_{eval} is the ground truth of the dataset consisting of a point (i.e., a marker) near the middle of each cell in the evaluation region.

In our evaluations, we follow the conventions described in [25]. We accepted a cell as correctly segmented if it contains strictly one ground truth point (i.e., a marker), and has at least 85% of its body inside the evaluation region. Any detected region outside the evaluation region, overlapping the evaluation region by less than 25% of the average region size, or touching image borders, was discarded.

Moreover, we compute cell area without taking into account the one pixel wide line that delineates cells in the segmentation.

For validating the quantifications, we also use the relative error , defined as:

$$\delta x = \frac{\Delta x}{x} = \frac{x_0 - x}{x} \tag{9}$$

where x is the true value of the quantity, x_0 the measured or inferred value, and Δx the estimation error. Relative error statistics such as minimum (Min), maximum (Max), and mean (Mean) value, first, second and third quartiles (i.e., Q1, Median, and Q3), and the interquartile range (IQR) are also computed.

Shared variation among data is assessed through correlation coefficients (r) and the coefficient of determination (R^2) with associated p-value. Data are interval (Pearson's correlation coefficient requires interval or ratio data), and normality is checked graphically (using QQ-plots) as well as quantitatively using D'Agostino - Pearson omnibus, Shapiro - Wilk, and Lilliefors tests. If normality is true, Pearson's correlation coefficient is applied. If the data are non-normal, Spearman's correlation coefficient is calculated.

Cell count

The results of cell counting from the proposed method in this work are compared against the measurements from the software NAVIS and Vigueras-Guillén et al. ([29]) using manual measurements as ground truth. Preceding a quantitative comparison of the correlation coefficients of the data, normality tests have been applied. Thus, Table 1 shows the results of three different normality tests. Using 0.05 as the criterion for significance, the ground truth, Vigueras-Guillén et al., and the proposed method's results can be associated with a normal distribution (p-value > 0.05), whereas the NAVIS software's results can not (p-value < 0.05). The QQ-plots of Figure 13 confirm the normal distribution associated with the proposed method, Vigueras-Guillén et al., and the ground truth, and the non-normal distribution associated with the NAVIS data because several of its measurements deviate considerably from the line. In the proposed method, Vigueras-Guillén et al., and ground truths' QQ-plots, the points approximately lie on a line, thus their distributions are linearly related.

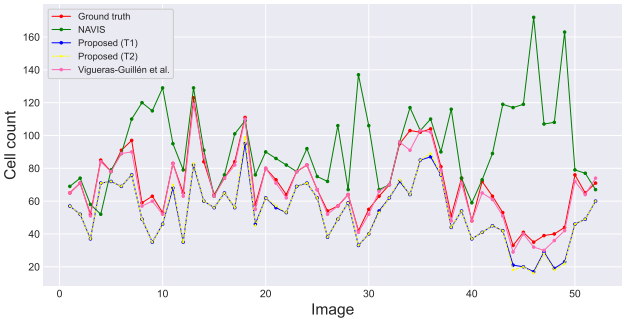

Figure 12: Cell count sample plots.

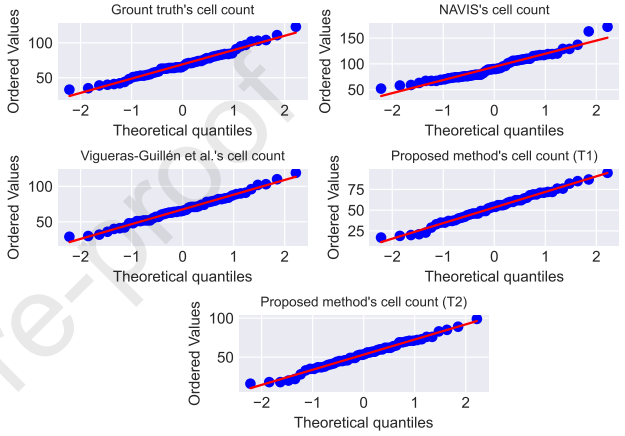

Figure 13: QQ-plots (Quantile-Quantile plots) for graphical testing the normality in cell count data: if the data lie on a line, they are considered normally distributed.

Hence, attending to the normality test results, Pearson's correlation coefficient can be applied to the ground truth, Vigueras-Guillén et al., and proposed method's data, whereas Spearman's correlation coefficient could be used regarding the correlation analysis of the NAVIS results.

Cell count results of the proposed method outperform those from the software NAVIS when their correlation statistics are compared. High correlation ($r = 0.907$) with high significance (p-value < 0.01) can be observed between the proposed method's results and the ground truth's data, similar to the state of the art method Vigueras-Guillén et al. [29]. The proposed method's results share 82.3% -proposed (T1)- and 82.7% -proposed (T2)- of the ground truth's variability (see Table 2).

Furthermore, the proposed method has a lower relative error than the software NAVIS in comparison to the ground truth (see Table 3). Also, visual inspection of Figure 12, Figure 14, and Figure 15 shows that the proposed segmentation method produces counting results that are closer to the ground truth than the NAVIS counting results, and approaches to the state of the art method Vigueras-Guillén et al. [29] which presents the best results.

Table 1
p-values for checking the normality of cell count data

Method	D'Agostino-Pearson	Shapiro-Wilk	Lilliefors
Proposed (T2)	0.979	0.874	0.99
Proposed (T1)	0.871	0.869	0.99
Vigueras-Guillén et al.	0.727	0.872	0.99
Ground truth	0.394	0.504	0.502
NAVIS	0.019	0.0153	0.0391

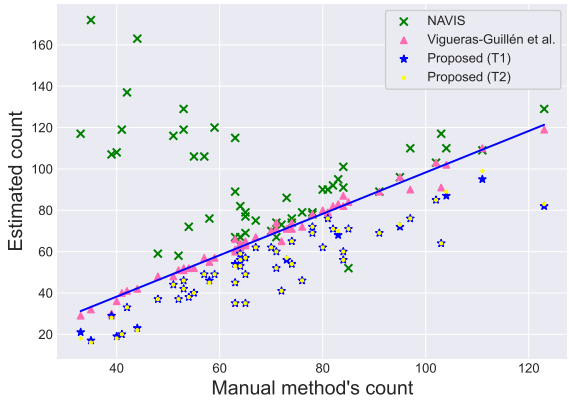

Figure 14: Cell count scatter plot.

Table 2
Cell count correlation coefficient statistics

Method	r	R^2	p-value
Vigueras-Guillén et al.	0.991	0.982	$1.484e{-}45$
Proposed (T2)	0.909	0.827	1.164e-20
Proposed (T1)	0.907	0.823	$2.041e{-}20$
NAVIS	-0.130	0.017	0.358

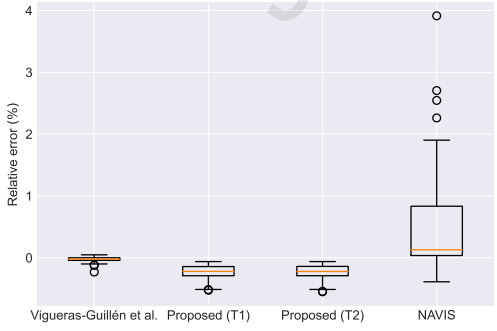

Figure 15: Relative errors in cell counting in the proposed method and the software NAVIS.

Cell density

In the graphical test of normality of Figure 17, it can be seen that all methods have an approximately normal distribution. Quantitatively, the normality of the cell density data is confirmed with *p*-values greater than 0.05 for all methods (Vigueras-Guillén et al., ground truth, NAVIS, Selig et al., and the proposed method) (see Table 4). Hence, we apply Pearson's correlation coefficient to cell density data for evaluating the variability they share with the ground truth data.

Table 3
Cell count relative error statistics (first part)

Method	Min	Max	Mean
Vigueras-Guillén et al.	-0.231	0.048	-0.029
Proposed (T1)	-0.525	-0.062	-0.241
Proposed (T2)	-0.55	-0.062	-0.244
NAVIS	-0.388	3.914	0.534

Table 3
Cell count relative error statistics (continued)

Method	Q1	Median	Q3	IQR
Vigueras-Guillén et al.	-0.042	-0.023	0.0	0.042
Proposed (T1)	-0.29	-0.221	-0.142	0.148
Proposed (T2)	-0.29	-0.222	-0.14	0.15
NAVIS	0.036	0.13	0.834	0.798

Table 4
p-values for checking cell density data normality

Method	D'Agostino-Pearson	Shapiro-Wilk	Lilliefors
Proposed (T1)	0.493	0.418	0.642
Selig et al.	0.457	0.300	0.823
Proposed (T2)	0.454	0.359	0.663
Ground truth	0.430	0.215	0.696
NAVIS	0.129	0.252	0.526
Vigueras-Guillén et al.	0.439	0.177	0.477

The sample plots of Figure 16, the scatter plots of Figure 18 and Figure 19, and the error plot of Figure 20 show that our proposed method measures the cell density more accurately than the NAVIS software's method, and approaches the state of the art methods. Quantitatively, Table 5 shows high correlation coefficients (r) and coefficients of determination (R^2) for Vigueras-Guillén et al.'s results, Selig et al.'s results, and the proposed method's results (a shared variability with the ground truth of 99.7%, 99.2%, and [93.3% and 93.1%] respectively), that are higher than the respective NAVIS software's measures (a shared variability with the ground truth of 15.42%). The significance value of a test strengthens the results because in all cases the correlation coefficients are significant (p-value < 0.05), and in Vigueras-Guillén et al., Selig et al. and proposed methods they are highly significant (p-value $<< 0.01$). Furthermore, the estimated error of NAVIS software's method depends on the cell density whereas the proposed method produces a negative increase of the error with higher cell densities (see Figure 19). The box-plots of Figure 20 show that the proposed method has lower relative error than the method of the software NAVIS in comparison to the ground truth, and that is close to Vigueras-Guillén et al. and Selig et al. results (see

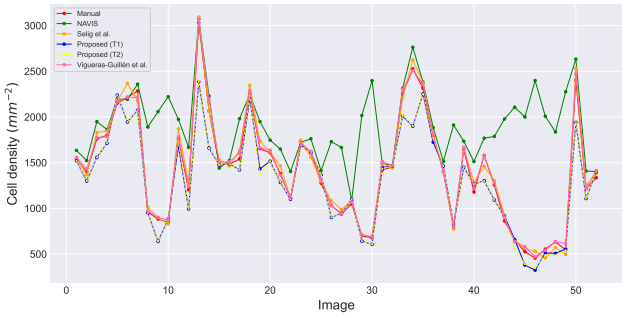

Figure 16: Cell density sample plots for visual inspection.

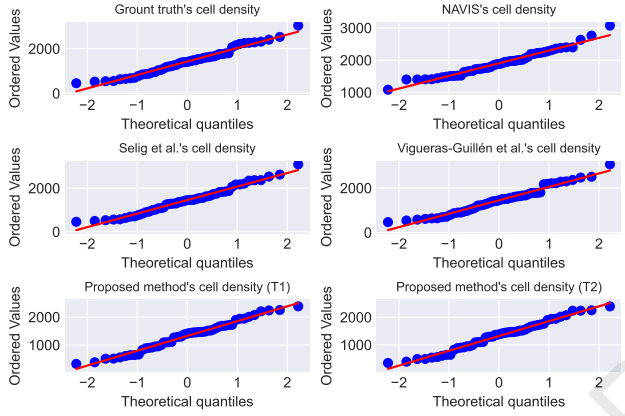

Figure 17: QQ-plots (Quantile-Quantile plots) for graphical testing the normality in cell density data: if the data lie on a line, they are considered normally distributed.

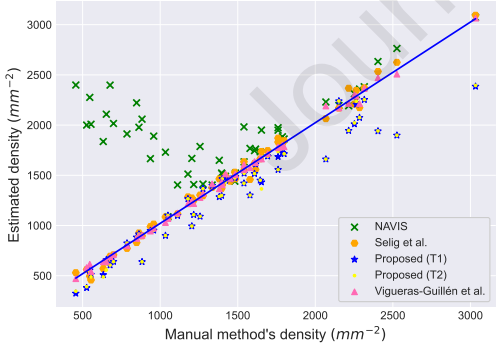

Figure 18: Estimated cell density compared with manually obtained density estimates.

also Table 6). Like in Vigueras-Guillén et al. ([29]) and Selig et al. ([25]) methods, the proposed method in this work improves cell density computation results comparing to the software NAVIS.

Cell polymegatism

The graphical test of normality in Figure 21 shows that the Vigueras-Guillén et al. ([29]), ground truth and the proposed method polymegathism data can be considered to have a normal distribution. The NAVIS and Selig's methods, although close, deviate away from the line, and cannot be considered as having the normal distribution.

Quantitatively, Table 7 shows a p-value > 0.05 for the ground truth, Vigueras-Guillén et al. and the proposed method, confirming its high probability to be normally distributed. Thus, Pearson's correlation coefficient can be used for as-

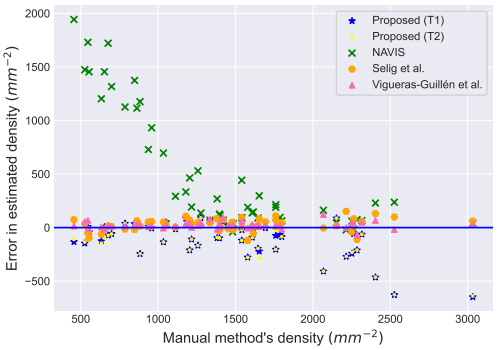

Figure 19: Error in estimated cell density vs. manually obtained density estimates.

Table 5
Cell density correlation coefficient statistics

Method	r	R^2	p-value
Vigueras-Guillén et al.	0.999	0.997	$3.6643e-66$
Selig et al.	0.996	0.992	$1.3615e-53$
Proposed (T1)	0.966	0.933	$5.2164e-31$
Proposed (T2)	0.965	0.931	$1.0549e-30$
NAVIS	0.393	0.154	$3.9789e-03$

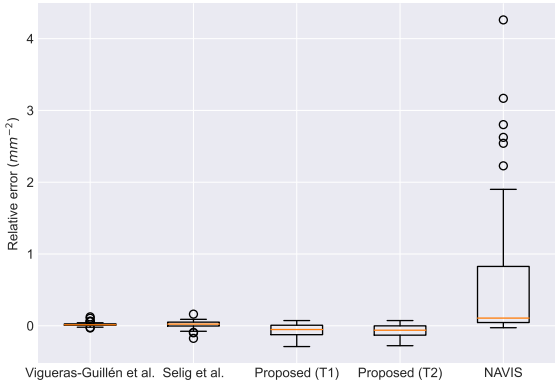

Figure 20: Relative error in cell density estimation in the proposed method, the software NAVIS and Selig's method.

Table 6
Cell density relative error statistics (first part)

Method	Min	Max	Mean
Selig et al.	-0.175	0.162	0.017
Vigueras-Guillén et al.	-0.031	0.125	0.018
Proposed (T1)	-0.289	0.073	-0.067
Proposed (T2)	-0.277	0.073	-0.071
NAVIS	-0.027	4.261	0.639

Table 6
Cell density relative error statistics (continued)

Method	Q1	Median	Q3	IQR
Selig et al.	-0.003	0.023	0.051	0.054
Vigueras-Guillén et al.	0.007	0.014	0.027	0.02
Proposed (T1)	-0.124	-0.052	0.008	0.132
Proposed (T2)	-0.131	-0.062	-0.001	0.13
NAVIS	0.045	0.107	0.827	0.782

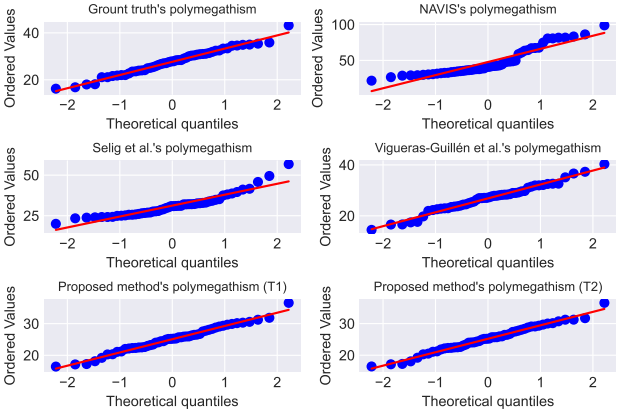

Figure 21: QQ-plots (Quantile-Quantile plots) for graphical testing the normality in polymegathims data: if the data lie on a line, they are considered normally distributed.

Table 7
p-values for checking polymegathism data normality

Method	D'Agostino-Pearson	Shapiro-Wilk	Lilliefors
Proposed (T2)	0.928	0.888	0.99
Ground truth	0.900	0.773	0.99
Proposed (T1)	0.806	0.854	0.965
Vigueras-Guillén et al.	0.809	0.682	0.487
NAVIS	0.019	$4.826e-05$	$1.000e{-}03$
Selig et al.	$2.151e-05$	$2.070e-04$	$9.835e{-}03$

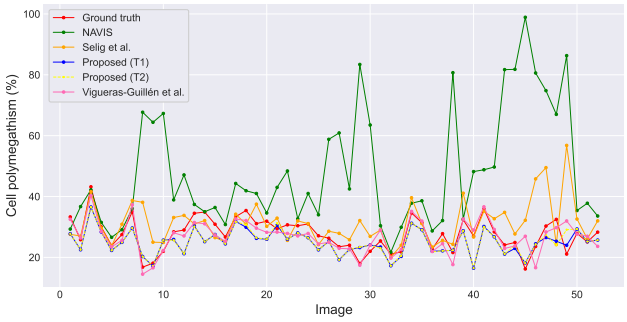

Figure 22: Sample plots of estimated polymegathism by the proposed method, the software NAVIS and Selig's method.

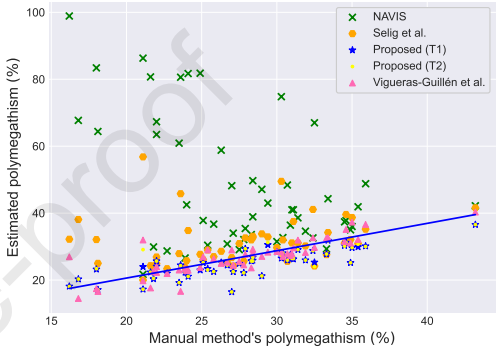

Figure 23: Cell polymegathism estimated by the proposed method, the software NAVIS and Selig's method.

Table 8
Polymegathism correlation coefficient statistics

Method	r	R^2	p-value
Vigueras-Guillén et al.	0.842	0.710	$4.963e-15$
Proposed (T1)	0.808	0.652	$4.604e-13$
Proposed (T2)	0.766	0.586	$3.835e-11$
Selig et al.	0.365	0.133	$7.870e-03$
NAVIS	-0.274	0.075	$4.960e-02$

sessing the correlation between Vigueras-Guillén et al., the proposed method, and the ground truth. Spearman's correlation coefficient should be used with the NAVIS and Selig et al.'s methods because they can be considered to have a non-normal distribution (p-value < 0.05, confirming the graphical test of normality in Figure 21).

The polymegathism sample plot in Figure 22, scatter plots in Figure 23, Figure 24, and Figure 25, and the error box plot in Figure 26 show an overall improvement of the proposed method when compared to the results of NAVIS and Selig et al.'s method. Quantitatively, in Table 8 the correlation coefficient (r value of 0.808 and 0.766) confirms a high correlation between the results of the proposed method and the ground truth. Furthermore, the proposed method can account for 65.52% and 58.6% (R^2 value of 0.652 and 0.586) of ground truth's variation, with an associated p-value < 0.01, thus the correlation coefficient is significant and indicates a genuine relationship between the results of the proposed method and the ground truth. Also, in Figure 23 a lower dispersion (lower deviation from a line) of the proposed method can be observed in comparison to the software NAVIS and Selig's method. In Figure 24 and Figure 25, a lower dependence can be appreciated of the estimated polymegathism error regarding manual polymegathism and manual cell density respectively in comparison to the software NAVIS and Selig's method ([25]). The results of our proposed method yield the lowest relative error (see Figure 26 and Table 9) after Vigueras-Guillén et al., which leads the results. In all polymegathism measures, our proposed method is close to those of Vigueras-Guillén et al.

Cell pleomorphism

The graphical test of normality in Figure 28 shows that the pleomorphism data can be considered to have a normal distribution. Quantitatively, the p-values of the Vigueras-

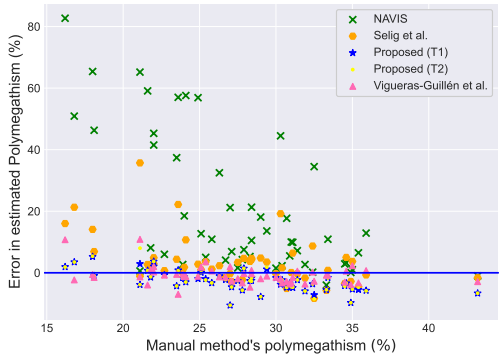

Figure 24: Error in estimated polymegathism in comparison with the manual polymegathism.

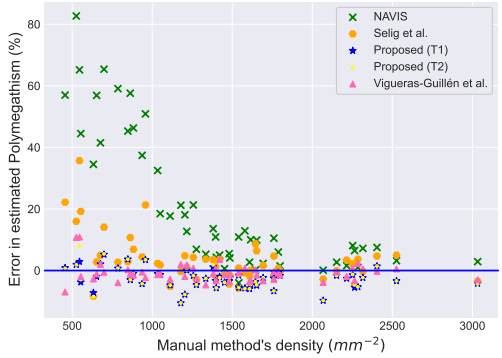

Figure 25: Error in estimated Polymegathism in comparison with manual density.

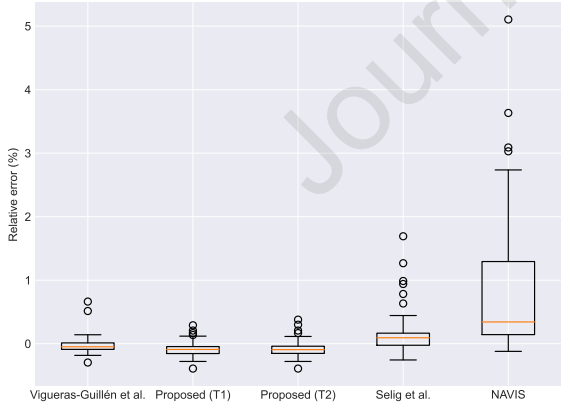

Figure 26: Relative error in polymegathism estimation in the proposed method, the software NAVIS and Selig's method.

Guillén et al., ground truth, Selig et al., and proposed methods are over 0.05, thus confirming the preceding consideration (see Table 10). For the NAVIS software's method, D'Agostino-Pearson's normality test determines a non-normal distribution (p-value < 0.05), whereas the Shapiro-Wilk and Lilliefors tests determine a normal distribution (p-value > 0.05) (two out of three tests) (see Table 10). By visual inspection of Figure 28, it can be assumed that the dots of the NAVIS method's QQ-plot for pleomorphism data deviate from the line to a similar extent as the other methods. Hence, we classify the NAVIS method's data as normally distributed. Thus, Pearson's correlation coefficient is applied to all pleomorphism data for assessing the correlation and variability they share with the ground truth data.

The sample plot in Figure 27 shows the results of the pleomorphism measure. Large dispersion (i.e., deviation from a line) is observable in scatter plots of Figure 29, Figure 30, and Figure 31, with an error dependent on the cell density in all cases (see Figure 31). This dispersion is reflected in Table 11 and the relative error boxplots in Figure 32. The

Table 9
Cell polymegathism relative error statistics (first part)

Method	Min	Max	Mean
Vigueras-Guillén et al.	-0.296	0.664	-0.021
Proposed (T2)	-0.391	0.379	-0.073
Proposed (T1)	-0.391	0.291	-0.079
Selig et al.	-0.255	1.692	0.169
NAVIS	-0.12	5.105	0.886

Table 9
Cell polymegathism relative error statistics (continued)

Method	Q1	Median	Q3	IQR
Vigueras-Guillén et al.	-0.089	-0.048	0.013	0.102
Proposed (T2)	-0.152	-0.093	-0.039	0.113
Proposed (T1)	-0.155	-0.09	-0.045	0.11
NAVIS	0.143	0.343	1.294	1.151
Selig et al.	-0.024	0.094	0.166	0.19

Table 10
p-values for checking pleomorphism data normality

Method	D'Agostino-Pearson	Shapiro-Wilk	Lilliefors
Ground truth	0.843	0.322	0.467
Proposed (T1)	0.641	0.441	0.405
Proposed (T2)	0.365	0.444	0.257
Selig et al	0.325	0.148	0.196
Vigueras-Guillén et al.	0.150	0.076	0.324
NAVIS	0.016	0.072	0.386

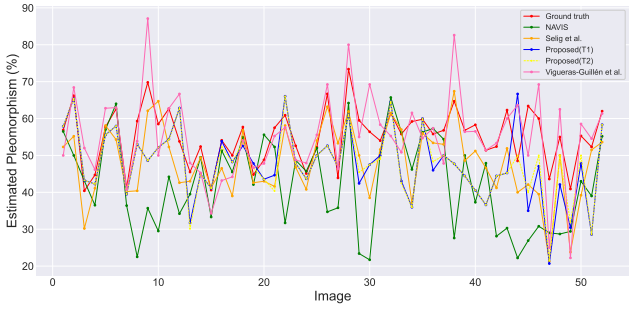

Figure 27: Sample plots of estimated cell pleomorphism by the proposed method, the software NAVIS and Selig's method.

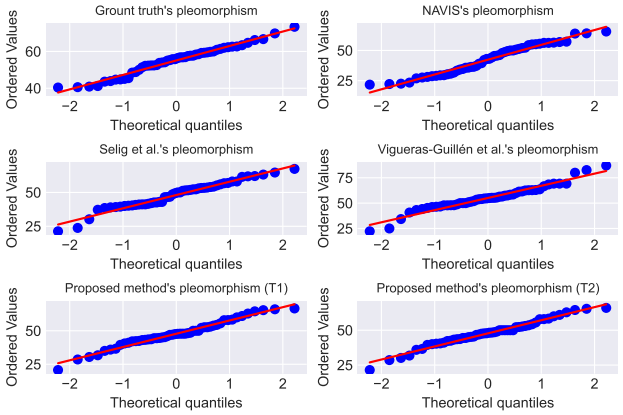

Figure 28: QQ-plots (Quantile-Quantile plots) for graphical testing the normality in pleomorphism data: if the data lie on a line, they are considered normally distributed.

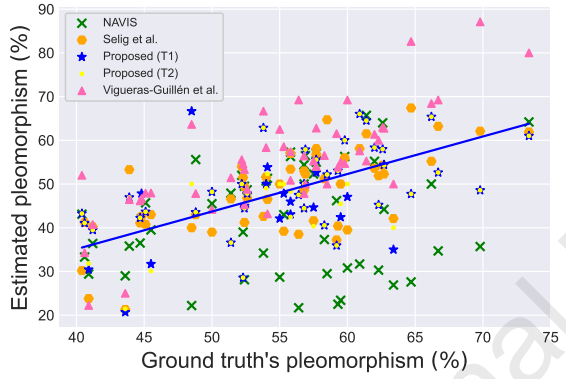

Figure 29: Estimated pleomorphism in comparison with manual pleomorphism.

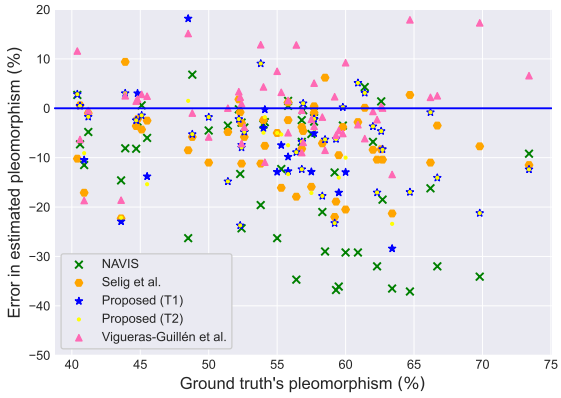

Figure 30: Error in estimated pleomorphism in comparison with manual pleomorphism.

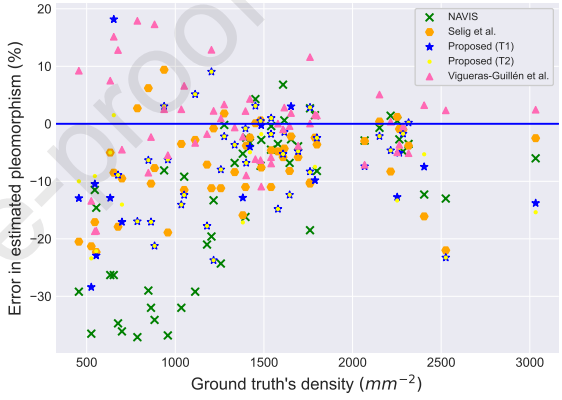

Figure 31: Error in estimated pleomorphism in comparison with manual density.

proposed method is closer to the positive correlation (r) of Selig et al. and Vigueras-Guillén et al. methods ([0.492 and 0.566] vs. 0.682, and 0.768 respectively), and it accounts for [24.2 and 32] % of shared variability (R^2) with the ground truth versus the 46.5% and 58.9% of Selig et al. and Vigueras-Guillén et al. methods respectively. In those cases, the associated p-value < 0.01 supports a significant correlation coefficient whereas the NAVIS method has a non-significant correlation coefficient (see Table 11). The proposed method has a lower error than the NAVIS method and it is close to that of Selig's method [25] (see Figure 32 and Table 12). However, it should be pointed out that in all cases the errors are larger than the errors computed for the other clinical parameters quantified in this work.

Table 11
Pleomorphism correlation coefficient statistics

Method	r	R^2	p-value
Vigueras-Guillén et al.	0.768	0.589	$3.183e-11$
Selig et al.	0.682	0.465	$2.562e-08$
Proposed (T2)	0.566	0.320	$1.226e-05$
Proposed (T1)	0.492	0.242	$2.113e-04$
NAVIS	0.188	0.035	$1.831e-01$

F-Measure

The F-measure quantity is not available in the ground truth of the used data set, but [25] provides its F-measure results. Hence, we include F-measure comparisons against the results from [25] for completeness. In [25], the mean F-measure is also calculated for segmentation results obtained using the methods described in [31] and [7]. The mean F-measure value obtained by our proposed method surpasses the value from [7], is similar to the one from [31], and close to the mean F-measure reported in [25] (see Table 13). Charts of the F-measure values of Selig et at.'s method and our proposed method can be seen in Figure 33 and Figure 34.

4. Discussion

Concerning the used dataset, we have modified some aspects of it for its use in this work. A hole was filled in images 34 and 48 named as "gt_region*.png" representing ROIs. Also, we remove a narrow bar that doesn't contour any cell in the ROI of image 48 (see Figure 35).

In the images (of the used data set) that contain marks approximately in the center of each cell, there are points

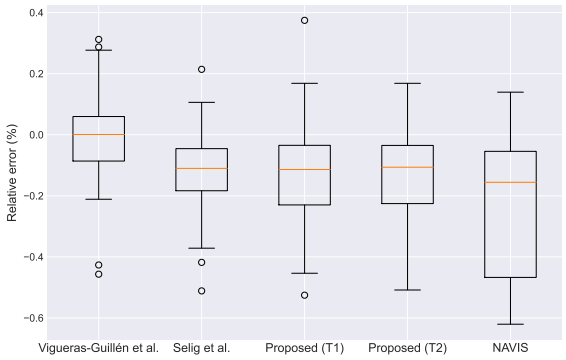

Figure 32: Relative error in pleomorphism estimation in the proposed method, the software NAVIS and Selig's method.

Table 12
Cell pleomorphism relative error statistics (first part)

Method	Min	Max	Mean
Vigueras-Guillén et al.	-0.457	0.312	-0.004
Selig et al.	-0.511	0.214	-0.127
Proposed (T1)	-0.525	0.375	-0.128
Proposed (T2)	-0.509	0.168	-0.129
NAVIS	-0.621	0.139	-0.222

Table 12
Cell pleomorphism relative error statistics (continued)

Method	Q1	Median	Q3	IQR
Vigueras-Guillén et al.	-0.086	0.001	0.06	0.146
Selig et al.	-0.183	-0.11	-0.046	0.137
Proposed (T1)	-0.23	-0.114	-0.035	0.195
Proposed (T2)	-0.226	-0.106	-0.035	0.191
NAVIS	-0.467	-0.156	-0.054	0.413

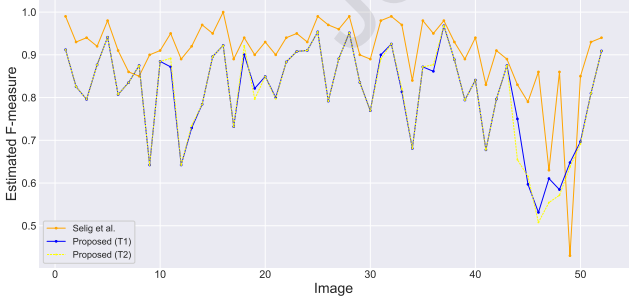

Figure 33: Estimated F-measure by the proposed approach and Selig's method.

(i.e., marked cells) placed outside the corresponding ROI. To the best of our knowledge, it happens in images 41, 47, and 48. Also, in the accompanying CSV file that contains the morphometrics computed in a manually assisted manner, the data corresponding to images 4, 8, 12, 21, 22, 26, 34, and 36 regarding the manual count of cells, does not match the number of marks placed by an expert near the center of each cell in the respective ROI. Hence, in this work, we used as

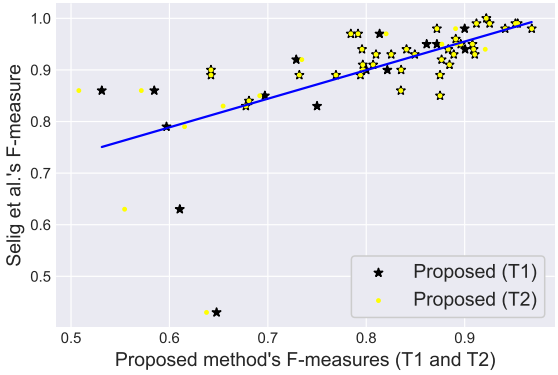

Figure 34: Proposed method F-measure in comparison with Selig's F-measure.

Table 13
Mean F-measure values over all images

Method	$F-measure$
Selig et al.	0.907
Vincent et al. [31]	0.821
Proposed (T1)	0.813
Proposed (T2)	0.810
Gavet et al. [7]	0.722

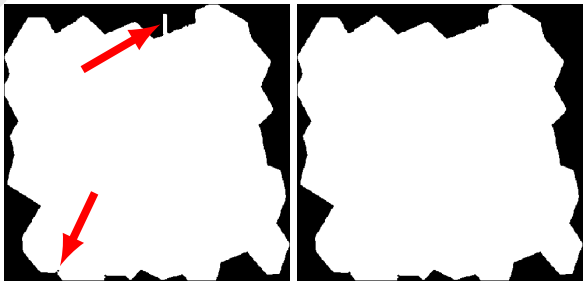

Figure 35: A sample of changes made in this work to a ROI image. (a) a hole inside the ROI and a bar getting out of the ROI pointed by arrows, (b) corrections on the hole and the bar in (a).

ground truth the point-markers placed by an expert near the center of each cell, strictly inside the ROI.

Regarding the frequency analysis, the fact that the mean cell area is obtained from the 2DFFT analysis (i.e., see subsubsection 2.1.2) of corneal endothelium images, without any user intervention (i.e., fully automatic), is a motivation factor to its use for removing the artifacts in the binary images.

The similar size of the cells in normal corneal endothelium [5, 32, 23, 24, 1], (i.e., small variability in cell area) is a motivation to use thresholding for removing artifacts in the binary images. Although the used images are not from the normal endothelium, and in practice "cells of different shape and size can be seen" [18] (see Figure 2), due to inherent issues of the image capture process, cells might ap-

pear merged which increases their area as foreground objects. Another important remark is that with aging corneal cells die and neighboring cells tend to elongate to fill in the space left by the dead cell, resulting in many cells becoming bigger [31, 24].

Thus, we tested the automatically found mean cell area as a threshold value for removing artifacts on the binary image. The experiments showed that the loss of the smallest cells in some images is possible (the mean cell area is too large to be used as the threshold value in some cases, hence the necessity of a scaled-down version of it). But, how much to reduce its value? We found a possible solution empirically.

It is known that the central ring radius of the image frequency spectrum is inversely proportional to the cell size of the image. Therefore, the mean cell area was divided by the numeric value of the radius of the central ring associated with the characteristic frequency (f^*) of the image frequency spectrum (i.e., n_{rf^*}, see Equation 4). Only the radius numeric value is needed because we are not establishing a relationship between the cell mean area and the ring radius, but only scaling down the area. Hence, we will have a threshold value with squared dimension that is useful for thresholding by area the connected component in the binary image.

Consequently, the division produced a scaled-down mean cell area value which we have proved (empirically, in the 52 images of the used data set) can be used as a threshold for removing the artifacts in the obtained binary images.

We tested another threshold value by scaling down the mean cell area by the area of the frequency spectrum ring pattern at f^*. Experiments showed that a scaling-up coefficient is needed to achieve the artifact removal task. We found empirically a fixed value for the coefficient of 30.886 that is capable of producing the desired results, although further studies involving larger data sets are needed (see Equation 5).

This way, the artifacts, which are many times smaller than an endothelial cell, can be removed automatically using a global adaptive threshold value per image without significant loss of cells (e.g., see Figure 2), and it is reflected in the results (see section 3 and section 5).

The simplicity of the proposed method is an advantage, although it still relies on some empirically chosen thresholds, which represents a drawback because their validity is limited to the used data set. Also, the selection of the inscribed circles representing cells, although fully automatic, fails in some cases such as those when cells appear widely merged. Nevertheless, this first non-optimized version of the proposed method shows its possibilities by the experimental results, and we want to investigate it further. Automatically finding the minimum cell area per image through frequency analysis could be a solution we aim to avoid the empirical threshold selection.

5. Conclusions

In this work, we introduced a method for segmenting endothelial cells in CM images of the human cornea. We showed that corneal endothelium confocal binary images can be automatically obtained in two steps: DoG filtering and thresholding using the minimum value of the DoG filtered image intensity. We automatically computed the mean cell area using frequency analysis and divided it by the the numeric value of the radius of the ring pattern of the image spectrum associated with the characteristic frequency. This value proved a valid, global, adaptive, and automatic threshold per binary image to remove artifacts. A second effective and automatic threshold for artifact removal was obtained (through dividing the mean cell area by the area of the aforementioned ring pattern and scaling-up this ratio by a coefficient of 30.886) and tested on the used data set. Through the experimentation we have shown that both proposed equations for threshold value computation produced similar valid results. Inscribing circles in the foreground objects of the distance map of the free of artifacts binary image proved a valid method to achieve single-cell detection. Although we determined empirically a threshold value for selecting the circle centers, the proposed method produced results of sufficient accuracy compared to the used data-set outcomes. Our method gives better results than the microscope software (i.e., NAVIS). Also, our estimated polymegathism has lower error and scatters, with better correlation than the state-of-the-art segmentation method Selig et al. ([25]). In all other cases, our results are close to the state-of-the-art methods comparing to the ground truth. With the obtained results, we show the method's potential, and we expect to improve it (e.g., by automatically selecting the empirically chosen threshold values) for stimulating its effective application in clinical settings.

Conflict of interest statement

The authors declare that they have no known competing financial interests or personal relationships that could have appeared to influence the work reported in this paper.

6. Acknowledgements

We thank to the Rotterdam Ophthalmic Institute, the Rotterdam Ophthalmic Data Repository (http://rod-rep.com) and Juan P. Vigueras-Guillén for their collaboration to dispel our doubts around the used data-set.

This work (or part of the work) was supported by the Special Research Fund (BOF) of Ghent University, Belgium, Grant Code 01W03516.

References

[1] Al-Fahdawi, S., Qahwaji, R., Al-Waisy, A.S., Ipson, S., Ferdousi, M., Malik, R.A., Brahma, A., 2018. A fully automated cell segmentation and morphometric parameter system for quantifying corneal endothelial cell morphology. Computer methods and programs in biomedicine 160, 11–23.

[2] Bucht, C., Söderberg, P., Manneberg, G., 2006. A model for corneal endothelial morphometry by diffraction., in: Proc. SPIE, pp. 61380O–61380O–8. URL: http://dx.doi.org/10.1117/12.660023, doi:10.1117/12.660023.

[3] Bucht, C., Söderberg, P., Manneberg, G., 2009. Fully automated corneal endothelial morphometry of images captured by clinical spec-

ular microscopy, in: Proc. SPIE, pp. 716315–716315–8. URL: http://dx.doi.org/10.1117/12.816850, doi:10.1117/12.816850.

[4] Fabijańska, A., 2017. Corneal endothelium image segmentation using feedforward neural network, in: 2017 Federated Conference on Computer Science and Information Systems (FedCSIS), pp. 629–637. doi:10.15439/2017F54.

[5] Foracchia, M., Ruggeri, A., 2004. Automatic estimation of endothelium cell density in donor corneas by means of fourier analysis. Medical and Biological Engineering and Computing 42, 725–731.

[6] Foster, C., Azar, D., Dohlman, C., 2005. Corneal endothelium. The cornea: scientific foundations and clinical practice. 4th ed Smolin and Thoft's, Ed Lippincott Williams & Wilkins, Philadelphia, PA, USA .

[7] Gavet, Y., Pinoli, J.C., 2008. Visual perception based automatic recognition of cell mosaics in human corneal endothelium microscopy images. Image Analysis & Stereology 27, 53–61. URL: http://www.ias-iss.org/ojs/IAS/article/view/830, doi:10.5566/ias.v27.p53-61.

[8] Gonzalez, R.C., Woods, R.E., 2005. Digital image processing third edition [m]. Beijing: Publishing House Of Electronics Industry .

[9] Gurevich, I.B., Yashina, V.V., Fedorov, A.A., Nedzved', A.M., Tleubaev, A.T., 2017. Development, investigation, and software implementation of a new mathematical method for automating the analysis of corneal endothelium images. Pattern Recognition and Image Analysis 27, 550–559. URL: https://doi.org/10.1134/S1054661817030130.

[10] Habrat, K., Habrat, M., Gronkowska-Serafin, J., Piórkowski, A., 2016. Cell Detection in Corneal Endothelial Images Using Directional Filters. Springer International Publishing, Cham. pp. 113–123. URL: http://dx.doi.org/10.1007/978-3-319-23814-2_14, doi:10.1007/978-3-319-23814-2_14.

[11] Hartmann, C., Köditz, W., 1984. Automated morphometric endothelial analysis combined with video specular microscopy. Cornea 3, 155–167.

[12] Herrera-Pereda, R., Taboada Crispi, A., Babin, D., Philips, W., Holsbach Costa, M., 2021. A review on digital image processing techniques for in-vivo confocal images of the cornea. Medical Image Analysis 73, 102188. URL: https://www.sciencedirect.com/science/article/pii/S1361841521002346, doi:https://doi.org/10.1016/j.media.2021.102188.

[13] Imre, L., Nagymihály, A., 2001. Reliability and reproducibility of corneal endothelial image analysis by in vivo confocal microscopy. Graefe's Archive for Clinical and Experimental Ophthalmology 239, 356–360. URL: http://dx.doi.org/10.1007/s004170100278, doi:10.1007/s004170100278.

[14] Kitzmann S, A., Winter J, E., Nau B, C., McLaren W, J., Hodge O, D., Bourne M, W., 2005. Comparison of Corneal Endothelial Cell Images From a Noncontact Specular Microscope and a Scanning Confocal Microscope. Cornea 24, 980–984. doi:10.1097/01.ico.0000159737.68048.97.

[15] Klais M.,C., C., Bühren, J., Kohnen, T., 2003. Comparison of Endothelial Cell Count Using Confocal and Contact Specular Microscopy. Ophthalmologica 217, 99–103. doi:10.1159/000068562.

[16] Kumar, K.K., Srinivasa, G., 2018. Comeal endothelium cell segmentation and count using k-means and watershed algorithms, in: 2018 Second International Conference on Advances in Electronics, Computers and Communications (ICAECC), pp. 1–7. doi:10.1109/ICAECC.2018.8479526.

[17] Patel, D.V., McGhee, C.N., 2013. Quantitative analysis of in vivo confocal microscopy images: A review. Survey of Ophthalmology 58, 466–475. URL: http://www.sciencedirect.com/science/article/pii/S0039625712003025, doi:http://dx.doi.org/10.1016/j.survophthal.2012.12.003.

[18] Piórkowski, A., Gronkowska-Serafin, J., 2015. Towards automated cell segmentation in corneal endothelium images, in: Image Processing & Communications Challenges 6. Springer, pp. 179–186.

[19] Piorkowski, A., Nurzynska, K., Gronkowska-Serafin, J., Selig, B., Boldak, C., Reska, D., 2017. Influence of applied corneal endothelium image segmentation techniques on the clinical parameters. Computerized Medical Imaging and Graphics 55, 13–27.

[20] Poletti, E., Ruggeri, A., 2014. Segmentation of corneal endothelial cells contour through classification of individual component signatures, in: XIII Mediterranean Conference on Medical and Biological Engineering and Computing 2013, Springer. pp. 411–414.

[21] Ruggeri, A., Grisan, E., Jaroszewski, J., 2005. A new system for the automatic estimation of endothelial cell density in donor corneas. British journal of ophthalmology 89, 306–311.

[22] Scarpa, F., Fiorin, D., Ruggeri, A., 2007. In Vivo Three-Dimensional Reconstruction of the Cornea from Confocal Microscopy Images, in: Engineering in Medicine and Biology Society, 2007. EMBS 2007. 29th Annual International Conference of the IEEE, pp. 747–750. doi:10.1109/IEMBS.2007.4352398.

[23] Scarpa, F., Ruggeri, A., 2015. Automatic segmentation of corneal endothelial cells by a genetic algorithm. Investigative Ophthalmology & Visual Science 56.

[24] Scarpa, F., Ruggeri, A., 2016. Automated morphometric description of human corneal endothelium from in-vivo specular and confocal microscopy, in: Proc. 38th Annual Int. Conf. of the IEEE Engineering in Medicine and Biology Society (EMBC), pp. 1296–1299. doi:10.1109/EMBC.2016.7590944.

[25] Selig, B., Vermeer, K.A., Rieger, B., Hillenaar, T., Hendriks, C.L.L., 2015. Fully automatic evaluation of the corneal endothelium from in vivo confocal microscopy. BMC Medical Imaging 15, 13. doi:10.1186/s12880-015-0054-3.

[26] Sharif, M.S., Qahwaji, R., Ipson, S., Brahma, A., 2015a. Medical image classification based on artificial intelligence approaches: A practical study on normal and abnormal confocal corneal images. Applied Soft Computing 36, 269–282.

[27] Sharif, M.S., Qahwaji, R., Shahamatnia, E., Alzubaidi, R., Ipson, S., Brahma, A., 2015b. An efficient intelligent analysis system for confocal corneal endothelium images. Computer methods and programs in biomedicine 122, 421–436.

[28] Tinku, A., Ray, A.K., 2005. Image Processing Principles and Applications. John Wiley & Sons, Inc.

[29] Vigueras-Guillén, J.P., Andrinopoulou, E., Engel, A., Lemij, H.G., van Rooij, J., Vermeer, K.A., van Vliet, L.J., 2018. Corneal endothelial cell segmentation by classifier-driven merging of oversegmented images. IEEE Transactions on Medical Imaging 37, 2278–2289.

[30] Vigueras-Guillén, J.P., Sari, B., Goes, S.F., Lemij, H.G., van Rooij, J., Vermeer, K.A., van Vliet, L.J., 2019. Fully convolutional architecture vs sliding-window CNN for corneal endothelium cell segmentation. BMC Biomedical Engineering 1.

[31] Vincent, L.M., Masters, B.R., 1992. Morphological image processing and network analysis of cornea endothelial cell images, in: Proc. SPIE 1769, Image Algebra and Morphological Image Processing III, pp. 212–226. URL: http://dx.doi.org/10.1117/12.60644.

[32] Zhivov, A., Stachs, O., Kraak, R., Stave, J., Guthoff, R.F., 2006. In Vivo Confocal Microscopy of the Ocular Surface. The Ocular Surface 4, 81–93. URL: http://www.sciencedirect.com/science/article/pii/S1542012412700307, doi:http://dx.doi.org/10.1016/S1542-0124(12)70030-7.

Appendix

In this section we expose the measures as well as the relative error (δ_x) and estimated error (Δx) variables associated to Equation 9, using the manual measures as ground truth and including the methods NAVIS, Selig et al. ([25]), Vigueras-Guillén et al. ([29]), and our proposed method. The used terminology is as follows: "Proposed(T1)" (the proposed method using threshold value T_1 for artifact removal) as "Prop(T1)", "Proposed(T2)" (the proposed method using threshold value T_2 for artifact removal) as "Prop(T2)", "Vigueras-Guillén et al." ([29]) as "JPVG etal", and "Selig et al." ([25]) as "Selig etal". Selig et al. ([25]) does not provide in their public data set the cell count results, hence it doesn't appear in the corresponding table.

Table 14
Endothelial cell count (ECC) results and associated errors

	Endothelial cell count (ECC) results and associated errors																															
Img	Manual	NAVIS	Δx_1	$\lvert\Delta x_1\rvert$	δ_{x1}	$\lvert\delta_{x1}\rvert$	Prop(T1)	Δx_2	$\lvert\Delta x_2\rvert$	δ_{x2}	$\lvert\delta_{x2}\rvert$	Prop(T2)	Δx_3	$\lvert\Delta x_3\rvert$	δ_{x3}	$\lvert\delta_{x3}\rvert$	JPVG etal	Δx_4	$\lvert\Delta x_4\rvert$	δ_{x4}	$\lvert\delta_{x4}\rvert$
0	65	69	4	4	0.062	0.062	57	-8	8	-0.123	0.123	57	-8	8	-0.123	0.123	65	0	0	0.000	0.000
1	71	74	3	3	0.042	0.042	52	-19	19	-0.268	0.268	52	-19	19	-0.268	0.268	71	0	0	0.000	0.000
2	52	58	6	6	0.115	0.115	37	-15	15	-0.288	0.288	37	-15	15	-0.288	0.288	51	-1	1	-0.019	0.019
3	85	52	-33	33	-0.388	0.388	71	-14	14	-0.165	0.165	71	-14	14	-0.165	0.165	84	-1	1	-0.012	0.012
4	78	79	1	1	0.013	0.013	72	-6	6	-0.077	0.077	72	-6	6	-0.077	0.077	78	0	0	0.000	0.000
5	91	89	-2	2	-0.022	0.022	69	-22	22	-0.242	0.242	69	-22	22	-0.242	0.242	89	-2	2	-0.022	0.022
6	97	110	13	13	0.134	0.134	76	-21	21	-0.216	0.216	76	-21	21	-0.216	0.216	90	-7	7	-0.072	0.072
7	59	120	61	61	1.034	1.034	49	-10	10	-0.169	0.169	49	-10	10	-0.169	0.169	57	-2	2	-0.034	0.034
8	63	115	52	52	0.825	0.825	35	-28	28	-0.444	0.444	35	-28	28	-0.444	0.444	60	-3	3	-0.048	0.048
9	53	129	76	76	1.434	1.434	46	-7	7	-0.132	0.132	46	-7	7	-0.132	0.132	52	-1	1	-0.019	0.019
10	83	95	12	12	0.145	0.145	68	-15	15	-0.181	0.181	70	-13	13	-0.157	0.157	83	0	0	0.000	0.000
11	65	79	14	14	0.215	0.215	35	-30	30	-0.462	0.462	35	-30	30	-0.462	0.462	63	-2	2	-0.031	0.031
12	123	129	6	6	0.049	0.049	82	-41	41	-0.333	0.333	83	-40	40	-0.325	0.325	119	-4	4	-0.033	0.033
13	84	91	7	7	0.083	0.083	60	-24	24	-0.286	0.286	60	-24	24	-0.286	0.286	87	3	3	0.036	0.036
14	64	63	-1	1	-0.016	0.016	56	-8	8	-0.125	0.125	56	-8	8	-0.125	0.125	63	-1	1	-0.016	0.016
15	74	76	2	2	0.027	0.027	65	-9	9	-0.122	0.122	65	-9	9	-0.122	0.122	74	0	0	0.000	0.000
16	84	101	17	17	0.202	0.202	56	-28	28	-0.333	0.333	56	-28	28	-0.333	0.333	82	-2	2	-0.024	0.024
17	111	109	-2	2	-0.018	0.018	95	-16	16	-0.144	0.144	99	-12	12	-0.108	0.108	110	-1	1	-0.009	0.009
18	58	76	18	18	0.310	0.310	46	-12	12	-0.207	0.207	45	-13	13	-0.224	0.224	55	-3	3	-0.052	0.052
19	80	90	10	10	0.125	0.125	62	-18	18	-0.225	0.225	62	-18	18	-0.225	0.225	80	0	0	0.000	0.000
20	73	86	13	13	0.178	0.178	56	-17	17	-0.233	0.233	57	-16	16	-0.219	0.219	71	-2	2	-0.027	0.027
21	64	82	18	18	0.281	0.281	53	-11	11	-0.172	0.172	53	-11	11	-0.172	0.172	62	-2	2	-0.031	0.031
22	78	78	0	0	0.000	0.000	69	-9	9	-0.115	0.115	69	-9	9	-0.115	0.115	78	0	0	0.000	0.000
23	82	92	10	10	0.122	0.122	71	-11	11	-0.134	0.134	71	-11	11	-0.134	0.134	82	0	0	0.000	0.000
24	67	75	8	8	0.119	0.119	62	-5	5	-0.075	0.075	62	-5	5	-0.075	0.075	67	0	0	0.000	0.000
25	54	72	18	18	0.333	0.333	38	-16	16	-0.296	0.296	38	-16	16	-0.296	0.296	52	-2	2	-0.037	0.037
26	57	106	49	49	0.860	0.860	49	-8	8	-0.140	0.140	49	-8	8	-0.140	0.140	57	0	0	0.000	0.000
27	64	67	3	3	0.047	0.047	59	-5	5	-0.078	0.078	59	-5	5	-0.078	0.078	64	0	0	0.000	0.000
28	42	137	95	95	2.262	2.262	33	-9	9	-0.214	0.214	33	-9	9	-0.214	0.214	41	-1	1	-0.024	0.024
29	55	106	51	51	0.927	0.927	40	-15	15	-0.273	0.273	40	-15	15	-0.273	0.273	52	-3	3	-0.055	0.055
30	63	67	4	4	0.063	0.063	54	-9	9	-0.143	0.143	53	-10	10	-0.159	0.159	66	3	3	0.048	0.048
31	70	70	0	0	0.000	0.000	62	-8	8	-0.114	0.114	62	-8	8	-0.114	0.114	70	0	0	0.000	0.000
32	95	96	1	1	0.011	0.011	72	-23	23	-0.242	0.242	73	-22	22	-0.232	0.232	96	1	1	0.011	0.011
33	103	117	14	14	0.136	0.136	64	-39	39	-0.379	0.379	64	-39	39	-0.379	0.379	91	-12	12	-0.117	0.117
34	102	103	1	1	0.010	0.010	85	-17	17	-0.167	0.167	85	-17	17	-0.167	0.167	103	1	1	0.010	0.010
35	104	110	6	6	0.058	0.058	87	-17	17	-0.163	0.163	89	-15	15	-0.144	0.144	102	-2	2	-0.019	0.019
36	81	90	9	9	0.111	0.111	76	-5	5	-0.062	0.062	76	-5	5	-0.062	0.062	79	-2	2	-0.025	0.025
37	51	116	65	65	1.275	1.275	44	-7	7	-0.137	0.137	44	-7	7	-0.137	0.137	48	-3	3	-0.059	0.059
38	74	74	0	0	0.000	0.000	54	-20	20	-0.270	0.270	54	-20	20	-0.270	0.270	71	-3	3	-0.041	0.041
39	48	59	11	11	0.229	0.229	37	-11	11	-0.229	0.229	37	-11	11	-0.229	0.229	48	0	0	0.000	0.000
40	72	73	1	1	0.014	0.014	41	-31	31	-0.431	0.431	41	-31	31	-0.431	0.431	65	-7	7	-0.097	0.097
41	63	89	26	26	0.413	0.413	45	-18	18	-0.286	0.286	45	-18	18	-0.286	0.286	61	-2	2	-0.032	0.032
42	53	119	66	66	1.245	1.245	42	-11	11	-0.208	0.208	42	-11	11	-0.208	0.208	51	-2	2	-0.038	0.038
43	33	117	84	84	2.545	2.545	21	-12	12	-0.364	0.364	18	-15	15	-0.455	0.455	29	-4	4	-0.121	0.121
44	41	119	78	78	1.902	1.902	20	-21	21	-0.512	0.512	20	-21	21	-0.512	0.512	40	-1	1	-0.024	0.024
45	35	172	137	137	3.914	3.914	17	-18	18	-0.514	0.514	16	-19	19	-0.543	0.543	32	-3	3	-0.086	0.086
46	39	107	68	68	1.744	1.744	29	-10	10	-0.256	0.256	28	-11	11	-0.282	0.282	30	-9	9	-0.231	0.231
47	40	108	68	68	1.700	1.700	19	-21	21	-0.525	0.525	18	-22	22	-0.550	0.550	36	-4	4	-0.100	0.100
48	44	163	119	119	2.705	2.705	23	-21	21	-0.477	0.477	22	-22	22	-0.500	0.500	42	-2	2	-0.045	0.045
49	76	79	3	3	0.039	0.039	46	-30	30	-0.395	0.395	46	-30	30	-0.395	0.395	72	-4	4	-0.053	0.053
50	65	77	12	12	0.185	0.185	49	-16	16	-0.246	0.246	49	-16	16	-0.246	0.246	64	-1	1	-0.015	0.015
51	71	67	-4	4	-0.056	0.056	60	-11	11	-0.155	0.155	60	-11	11	-0.155	0.155	74	3	3	0.042	0.042
min	33.000	52.000	-33.000	0.000	-0.388	0.000	17.000	-41.000	5.000	-0.525	0.062	16.000	-40.000	5.000	-0.550	0.062	29.000	-12.000	0.000	-0.231	0.000
max	123.000	172.000	137.000	137.000	3.914	3.914	95.000	-5.000	41.000	-0.062	0.525	99.000	-5.000	40.000	-0.062	0.550	119.000	3.000	12.000	0.048	0.231
mean	69.212	94.173	24.962	26.577	0.534	0.553	53.192	-16.019	16.019	-0.241	0.241	53.231	-15.961	15.961	-0.244	0.244	67.481	-1.731	2.154	-0.029	0.035

Table 15
Endothelial cell density (ECD) results ($cell/mm^2$) and associated errors

												Endothelium cell density (ECD) results and associated errors																			
Img	Manual	NAVIS	Δx_1	$\lvert\Delta x_1\rvert$	δ_{x1}	$\lvert\delta_{x1}\rvert$	Prop(T1)	Δx_2	$\lvert\Delta x_2\rvert$	δ_{x2}	$\lvert\delta_{x2}\rvert$	Prop(T2)	Δx_3	$\lvert\Delta x_3\rvert$	δ_{x3}	$\lvert\delta_{x3}\rvert$	JPVG etal	Δx_4	$\lvert\Delta x_4\rvert$	δ_{x4}	$\lvert\delta_{x4}\rvert$	Selig etal	Δx_5	$\lvert\Delta x_5\rvert$	δ_{x5}	$\lvert\delta_{x5}\rvert$					
0	1541	1634	93	93	0.060	0.060	1519.669	-21.331	21.331	-0.014	0.014	1519.669	-21.331	21.331	-0.014	0.014	1557	16	16	0.010	0.010	1553	12	12	0.008	0.008					
1	1396	1523	127	127	0.091	0.091	1298.597	-97.403	97.403	-0.070	0.070	1298.597	-97.403	97.403	-0.070	0.070	1433	37	37	0.027	0.027	1368	-28	28	-0.020	0.020					
2	1760	1949	189	189	0.107	0.107	1556.135	-203.865	203.865	-0.116	0.116	1556.135	-203.865	203.865	-0.116	0.116	1774	14	14	0.008	0.008	1831	71	71	0.040	0.040					
3	1799	1862	63	63	0.035	0.035	1713.553	-85.447	85.447	-0.047	0.047	1713.553	-85.447	85.447	-0.047	0.047	1784	-15	15	-0.008	0.008	1845	46	46	0.026	0.026					
4	2152	2196	44	44	0.020	0.020	2239.620	87.620	87.620	0.041	0.041	2239.620	87.620	87.620	0.041	0.041	2171	19	19	0.009	0.009	2169	17	17	0.008	0.008					
5	2215	2193	-22	22	-0.010	0.010	1944.941	-270.059	270.059	-0.122	0.122	1945.621	-269.379	269.379	-0.122	0.122	2215	0	0	0.000	0.000	2367	152	152	0.069	0.069					
6	2285	2359	74	74	0.032	0.032	2074.301	-210.699	210.699	-0.092	0.092	2074.705	-210.295	210.295	-0.092	0.092	2214	-71	71	-0.031	0.031	2174	-111	111	-0.049	0.049					
7	958	1890	932	932	0.973	0.973	952.189	-5.811	5.811	-0.006	0.006	952.189	-5.811	5.811	-0.006	0.006	974	16	16	0.017	0.017	1014	56	56	0.058	0.058					
8	883	2059	1176	1176	1.332	1.332	638.005	-244.995	244.995	-0.277	0.277	638.005	-244.995	244.995	-0.277	0.277	902	19	19	0.022	0.022	897	14	14	0.016	0.016					
9	848	2222	1374	1374	1.620	1.620	882.905	34.905	34.905	0.041	0.041	882.905	34.905	34.905	0.041	0.041	871	23	23	0.027	0.027	830	-18	18	-0.021	0.021					
10	1760	1974	214	214	0.122	0.122	1685.602	-74.398	74.398	-0.042	0.042	1736.033	-23.967	23.967	-0.014	0.014	1782	22	22	0.013	0.013	1870	110	110	0.062	0.062					
11	1204	1668	464	464	0.385	0.385	993.935	-210.065	210.065	-0.174	0.174	993.935	-210.065	210.065	-0.174	0.174	1242	38	38	0.032	0.032	1274	70	70	0.058	0.058					
12	3033	3073	40	40	0.013	0.013	2385.435	-647.565	647.565	-0.214	0.214	2394.792	-638.208	638.208	-0.210	0.210	3065	32	32	0.011	0.011	3094	61	61	0.020	0.020					
13	2068	2230	162	162	0.078	0.078	1660.596	-407.404	407.404	-0.197	0.197	1660.596	-407.404	407.404	-0.197	0.197	2190	122	122	0.059	0.059	2064	-4	4	-0.002	0.002					
14	1481	1441	-40	40	-0.027	0.027	1473.230	-7.770	7.770	-0.005	0.005	1473.230	-7.770	7.770	-0.005	0.005	1505	24	24	0.016	0.016	1531	50	50	0.034	0.034					
15	1485	1522	37	37	0.025	0.025	1486.576	1.576	1.576	0.001	0.001	1486.587	1.587	1.587	0.001	0.001	1509	24	24	0.016	0.016	1465	-20	20	-0.013	0.013					
16	1540	1982	442	442	0.287	0.287	1421.026	-118.974	118.974	-0.077	0.077	1420.054	-119.946	119.946	-0.078	0.078	1605	65	65	0.042	0.042	1635	95	95	0.062	0.062					
17	2264	2248	-16	16	-0.007	0.007	2206.601	-57.399	57.399	-0.025	0.025	2237.325	-26.675	26.675	-0.012	0.012	2288	24	24	0.011	0.011	2346	82	82	0.036	0.036					
18	1653	1950	297	297	0.180	0.180	1432.084	-220.916	220.916	-0.134	0.134	1464.627	-288.373	288.373	-0.174	0.174	1662	9	9	0.005	0.005	1737	84	84	0.051	0.051					
19	1608	1746	138	138	0.086	0.086	1516.417	-91.583	91.583	-0.057	0.057	1516.417	-91.583	91.583	-0.057	0.057	1637	29	29	0.018	0.018	1618	10	10	0.006	0.006					
20	1381	1649	268	268	0.194	0.194	1284.342	-96.658	96.658	-0.070	0.070	1289.169	-91.831	91.831	-0.066	0.066	1365	-16	16	-0.012	0.012	1464	83	83	0.060	0.060					
21	1112	1404	292	292	0.263	0.263	1098.384	-13.616	13.616	-0.012	0.012	1098.384	-13.616	13.616	-0.012	0.012	1124	12	12	0.011	0.011	1116	4	4	0.004	0.004					
22	1693	1723	30	30	0.018	0.018	1690.062	-2.938	2.938	-0.002	0.002	1690.062	-2.938	2.938	-0.002	0.002	1715	22	22	0.013	0.013	1746	53	53	0.031	0.031					
23	1615	1761	146	146	0.090	0.090	1610.475	-4.525	4.525	-0.003	0.003	1610.475	-4.525	4.525	-0.003	0.003	1625	10	10	0.006	0.006	1559	-56	56	-0.035	0.035					
24	1276	1412	136	136	0.107	0.107	1366.060	90.060	90.060	0.071	0.071	1366.060	90.060	90.060	0.071	0.071	1317	41	41	0.032	0.032	1296	20	20	0.016	0.016					
25	1034	1730	696	696	0.673	0.673	899.474	-134.526	134.526	-0.130	0.130	899.474	-134.526	134.526	-0.130	0.130	1029	-5	5	-0.005	0.005	1085	51	51	0.049	0.049					
26	937	1666	729	729	0.778	0.778	948.239	11.239	11.239	0.012	0.012	948.239	11.239	11.239	0.012	0.012	944	7	7	0.007	0.007	989	52	52	0.055	0.055					
27	1050	1087	37	37	0.035	0.035	1099.572	49.572	49.572	0.047	0.047	1099.572	49.572	49.572	0.047	0.047	1069	19	19	0.018	0.018	1074	24	24	0.023	0.023					
28	699	2016	1317	1317	1.884	1.884	640.648	-58.352	58.352	-0.083	0.083	639.566	-59.434	59.434	-0.085	0.085	711	12	12	0.017	0.017	708	9	9	0.013	0.013					
29	677	2398	1721	1721	2.542	2.542	605.441	-71.559	71.559	-0.106	0.106	605.347	-71.653	71.653	-0.106	0.106	689	12	12	0.018	0.018	694	17	17	0.025	0.025					
30	1421	1490	69	69	0.049	0.049	1448.167	27.167	27.167	0.019	0.019	1436.082	15.082	15.082	0.011	0.011	1514	93	93	0.065	0.065	1493	72	72	0.051	0.051					
31	1452	1471	19	19	0.013	0.013	1462.847	10.847	10.847	0.007	0.007	1462.847	10.847	10.847	0.007	0.007	1469	17	17	0.012	0.012	1441	-11	11	-0.008	0.008					
32	2252	2312	60	60	0.027	0.027	2010.427	-241.573	241.573	-0.107	0.107	2021.243	-230.757	230.757	-0.102	0.102	2301	49	49	0.022	0.022	2209	-43	43	-0.019	0.019					
33	2526	2763	237	237	0.094	0.094	1898.209	-627.791	627.791	-0.249	0.249	1898.209	-627.791	627.791	-0.249	0.249	2507	-19	19	-0.008	0.008	2625	99	99	0.039	0.039					
34	2316	2382	66	66	0.028	0.028	2253.238	-62.762	62.762	-0.027	0.027	2253.238	-62.762	62.762	-0.027	0.027	2365	49	49	0.021	0.021	2371	55	55	0.024	0.024					
35	1788	1884	96	96	0.054	0.054	1723.582	-64.418	64.418	-0.036	0.036	1765.929	-22.071	22.071	-0.012	0.012	1803	15	15	0.008	0.008	1816	28	28	0.016	0.016					
36	1400	1514	114	114	0.081	0.081	1464.083	64.083	64.083	0.046	0.046	1464.083	64.083	64.083	0.046	0.046	1405	5	5	0.004	0.004	1404	4	4	0.003	0.003					
37	786	1912	1126	1126	1.433	1.433	824.204	38.204	38.204	0.049	0.049	824.204	38.204	38.204	0.049	0.049	796	10	10	0.013	0.013	772	-14	14	-0.018	0.018					
38	1645	1735	90	90	0.055	0.055	1449.808	-195.192	195.192	-0.119	0.119	1451.028	-193.972	193.972	-0.118	0.118	1669	24	24	0.015	0.015	1664	19	19	0.012	0.012					
39	1179	1512	333	333	0.282	0.282	1264.704	85.704	85.704	0.073	0.073	1264.704	85.704	85.704	0.073	0.073	1216	37	37	0.031	0.031	1285	106	106	0.090	0.090					
40	1579	1768	189	189	0.120	0.120	1302.182	-276.818	276.818	-0.175	0.175	1301.284	-277.716	277.716	-0.176	0.176	1574	-5	5	-0.003	0.003	1458	-121	121	-0.077	0.077					
41	1257	1787	530	530	0.422	0.422	1090.636	-166.364	166.364	-0.132	0.132	1090.636	-166.364	166.364	-0.132	0.132	1278	21	21	0.017	0.017	1303	46	46	0.037	0.037					
42	863	1978	1115	1115	1.292	1.292	913.851	50.851	50.851	0.059	0.059	913.851	50.851	50.851	0.059	0.059	897	34	34	0.039	0.039	926	63	63	0.073	0.073					
43	653	2108	1455	1455	2.228	2.228	657.966	4.966	4.966	0.008	0.008	656.441	-96.559	96.559	-0.148	0.148	640	-13	13	-0.020	0.020	636	-17	17	-0.026	0.026					
44	526	2000	1474	1474	2.802	2.802	379.828	-146.172	146.172	-0.278	0.278	390.672	-135.328	135.328	-0.257	0.257	581	55	55	0.105	0.105	561	35	35	0.067	0.067					
45	456	2399	1943	1943	4.261	4.261	323.999	-132.001	132.001	-0.289	0.289	344.951	-111.049	111.049	-0.244	0.244	470	14	14	0.031	0.031	530	74	74	0.162	0.162					
46	554	2008	1454	1454	2.625	2.625	511.608	-42.392	42.392	-0.077	0.077	488.319	-65.681	65.681	-0.119	0.119	541	-13	13	-0.023	0.023	457	-97	97	-0.175	0.175					
47	633	1836	1203	1203	1.900	1.900	508.242	-124.758	124.758	-0.197	0.197	487.800	-145.200	145.200	-0.229	0.229	638	5	5	0.008	0.008	571	-62	62	-0.098	0.098					
48	546	2276	1730	1730	3.168	3.168	585.261	9.261	9.261	0.017	0.017	538.263	-7.737	7.737	-0.014	0.014	614	68	68	0.125	0.125	496	-50	50	-0.092	0.092					
49	2404	2633	229	229	0.095	0.095	1940.351	-463.649	463.649	-0.193	0.193	1941.697	-462.303	462.303	-0.192	0.192	2471	67	67	0.028	0.028	2534	130	130	0.054	0.054					
50	1216	1408	192	192	0.158	0.158	1107.138	-108.862	108.862	-0.090	0.090	1107.138	-108.862	108.862	-0.090	0.090	1218	2	2	0.002	0.002	1250	34	34	0.028	0.028					
51	1335	1403	68	68	0.051	0.051	1397.914	62.914	62.914	0.047	0.047	1397.914	62.914	62.914	0.047	0.047	1414	79	79	0.059	0.059	1379	44	44	0.033	0.033					
min	456.000	1087.000	-40.000	16.000	-0.027	0.007	323.999	-647.565	1.576	-0.289	0.001	344.951	-638.208	1.587	-0.277	0.001	470.000	-71.000	0.00	-0.031	0.000	457.000	-121.000	4.0	-0.175	0.002					
max	3033.000	3073.000	1943.000	1943.000	4.261	4.261	2385.435	90.060	647.565	0.073	0.289	2394.792	90.060	638.208	0.073	0.277	3065.000	122.000	122.00	0.125	0.125	3094.000	152.000	152.0	0.162	0.175					
mean	1426.808	1906.654	479.846	482.846	0.639	0.641	1323.315	-103.493	127.684	-0.067	0.088	1322.144	-104.664	127.843	-0.071	0.090	1449.019	22.212	28.25	0.018	0.023	1453.731	26.923	52.0	0.017	0.042					

Table 16
Endothelial cell polymegathism (CV) results (per cent [%] values) and associated errors

								Endothelial cell polymegathism (CV) results (in per cent [%] values) and associated errors															
Img	Manual	NAVIS	Δx_1	$\|\Delta x_1\|$	δ_{x1}	$\|\delta_{x1}\|$	Prop(T1)	Δx_2	$\|\Delta x_2\|$	δ_{x2}	$\|\delta_{x2}\|$	Prop(T2)	Δx_3	$\|\Delta x_3\|$	δ_{x3}	$\|\delta_{x3}\|$	JPVG etal	Δx_4	$\|\Delta x_4\|$	δ_{x4}	$\|\delta_{x4}\|$	Selig etal	Δx_5	$\|\Delta x_5\|$	δ_{x5}	$\|\delta_{x5}\|$
0	33.3	29.3	-4.0	4.0	-0.120	0.120	27.778	-5.522	5.522	-0.166	0.166	27.778	-5.522	5.522	-0.166	0.166	32.53	-0.77	0.77	-0.023	0.023	27.6	-5.7	5.7	-0.171	0.171
1	25.8	36.7	10.9	10.9	0.422	0.422	22.509	-3.291	3.291	-0.128	0.128	22.509	-3.291	3.291	-0.128	0.128	26.37	0.57	0.57	0.022	0.022	27.0	1.2	1.2	0.047	0.047
2	43.2	42.2	-1.0	1.0	-0.023	0.023	36.564	-6.636	6.636	-0.154	0.154	36.564	-6.636	6.636	-0.154	0.154	40.32	-2.88	2.88	-0.067	0.067	41.6	-1.6	1.6	-0.037	0.037
3	30.0	31.5	1.5	1.5	0.050	0.050	28.355	-1.645	1.645	-0.055	0.055	28.355	-1.645	1.645	-0.055	0.055	28.52	-1.48	1.48	-0.049	0.049	29.7	-0.3	0.3	-0.010	0.010
4	23.9	26.6	2.7	2.7	0.113	0.113	22.296	-1.604	1.604	-0.067	0.067	22.296	-1.604	1.604	-0.067	0.067	23.47	-0.43	0.43	-0.018	0.018	23.8	-0.1	0.1	-0.004	0.004
5	27.5	29.1	1.6	1.6	0.058	0.058	24.946	-2.554	2.554	-0.093	0.093	24.927	-2.573	2.573	-0.094	0.094	25.61	-1.89	1.89	-0.069	0.069	30.9	3.4	3.4	0.124	0.124
6	35.0	36.0	1.0	1.0	0.029	0.029	29.669	-5.331	5.331	-0.152	0.152	29.685	-5.315	5.315	-0.152	0.152	37.30	2.30	2.30	0.066	0.066	38.7	3.7	3.7	0.106	0.106
7	16.8	67.7	50.9	50.9	3.030	3.030	20.285	3.485	3.485	0.207	0.207	20.285	3.485	3.485	0.207	0.207	14.49	-2.31	2.31	-0.138	0.138	38.1	21.3	21.3	1.268	1.268
8	18.1	64.4	46.3	46.3	2.558	2.558	17.132	-0.968	0.968	-0.053	0.053	17.132	-0.968	0.968	-0.053	0.053	16.58	-1.52	1.52	-0.084	0.084	25.0	6.9	6.9	0.381	0.381
9	22.0	67.3	45.3	45.3	2.059	2.059	25.682	3.682	3.682	0.167	0.167	25.682	3.682	3.682	0.167	0.167	22.27	0.27	0.27	0.012	0.012	24.9	2.9	2.9	0.132	0.132
10	28.4	38.9	10.5	10.5	0.370	0.370	25.898	-2.502	2.502	-0.088	0.088	25.680	-2.720	2.720	-0.096	0.096	28.09	-0.31	0.31	-0.011	0.011	33.1	4.7	4.7	0.165	0.165
11	29.0	47.1	18.1	18.1	0.624	0.624	21.218	-7.782	7.782	-0.268	0.268	21.218	-7.782	7.782	-0.268	0.268	27.06	-1.94	1.94	-0.067	0.067	33.8	4.8	4.8	0.166	0.166
12	34.5	37.4	2.9	2.9	0.084	0.084	30.308	-4.192	4.192	-0.122	0.122	30.139	-4.361	4.361	-0.126	0.126	31.47	-3.03	3.03	-0.088	0.088	31.0	-3.5	3.5	-0.101	0.101
13	34.9	35.0	0.1	0.1	0.003	0.003	25.167	-9.733	9.733	-0.279	0.279	25.167	-9.733	9.733	-0.279	0.279	31.04	-3.86	3.86	-0.111	0.111	32.1	-2.8	2.8	-0.080	0.080
14	30.9	36.4	5.5	5.5	0.178	0.178	27.531	-3.369	3.369	-0.100	0.109	27.531	-3.369	3.369	-0.109	0.109	27.30	-3.60	3.60	-0.117	0.117	26.5	-4.4	4.4	-0.142	0.142
15	26.7	30.8	4.1	4.1	0.154	0.154	24.442	-2.258	2.258	-0.085	0.085	24.469	-2.231	2.231	-0.084	0.084	25.31	-1.39	1.39	-0.052	0.052	25.2	-1.5	1.5	-0.056	0.056
16	33.4	44.3	10.9	10.9	0.326	0.326	31.844	-1.556	1.556	-0.047	0.047	31.711	-1.689	1.689	-0.051	0.051	32.64	-0.76	0.76	-0.023	0.023	34.2	0.8	0.8	0.024	0.024
17	35.4	41.9	6.5	6.5	0.184	0.184	29.909	-5.491	5.491	-0.155	0.155	30.721	-4.679	4.679	-0.132	0.132	32.11	-3.29	3.29	-0.093	0.093	30.9	-4.5	4.5	-0.127	0.127
18	31.1	41.0	9.9	9.9	0.318	0.318	26.261	-4.839	4.839	-0.156	0.156	26.437	-4.663	4.663	-0.150	0.150	29.61	-1.49	1.49	-0.048	0.048	37.5	6.4	6.4	0.206	0.206
19	31.9	34.6	2.7	2.7	0.085	0.085	25.953	-5.947	5.947	-0.186	0.186	25.953	-5.947	5.947	-0.186	0.186	28.24	-3.66	3.66	-0.115	0.115	30.2	-1.7	1.7	-0.053	0.053
20	29.4	43.0	13.6	13.6	0.463	0.463	30.568	1.168	1.168	0.040	0.040	31.241	1.841	1.841	0.063	0.063	28.32	-1.08	1.08	-0.037	0.037	32.9	3.5	3.5	0.119	0.119
21	30.7	48.4	17.7	17.7	0.577	0.577	25.962	-4.738	4.738	-0.154	0.154	25.962	-4.738	4.738	-0.154	0.154	27.89	-2.81	2.81	-0.092	0.092	25.6	-5.1	5.1	-0.166	0.166
22	30.4	32.7	2.3	2.3	0.076	0.076	28.060	-2.340	2.340	-0.077	0.077	28.060	-2.340	2.340	-0.077	0.077	27.06	-3.34	3.34	-0.110	0.110	32.0	1.6	1.6	0.053	0.053
23	31.0	41.0	10.0	10.0	0.323	0.323	26.463	-4.537	4.537	-0.146	0.146	26.463	-4.537	4.537	-0.146	0.146	27.87	-3.13	3.13	-0.101	0.101	31.1	0.1	0.1	0.003	0.003
24	27.1	34.0	6.9	6.9	0.255	0.255	22.475	-4.625	4.625	-0.171	0.171	22.475	-4.625	4.625	-0.171	0.171	24.41	-2.69	2.69	-0.099	0.099	24.2	-2.9	2.9	-0.107	0.107
25	26.3	58.8	32.5	32.5	1.236	1.236	25.261	-1.039	1.039	-0.040	0.040	25.261	-1.039	1.039	-0.040	0.040	24.97	-1.33	1.33	-0.051	0.051	28.6	2.3	2.3	0.087	0.087
26	23.5	60.9	37.4	37.4	1.591	1.591	19.208	-4.292	4.292	-0.183	0.183	19.208	-4.292	4.292	-0.183	0.183	22.99	-0.51	0.51	-0.022	0.022	27.9	4.4	4.4	0.187	0.187
27	24.0	42.5	18.5	18.5	0.771	0.771	22.619	-1.381	1.381	-0.058	0.058	22.619	-1.381	1.381	-0.058	0.058	22.82	-1.18	1.18	-0.049	0.049	25.8	1.8	1.8	0.075	0.075
28	18.0	83.4	65.4	65.4	3.633	3.633	23.230	5.230	5.230	0.291	0.291	23.389	5.389	5.389	0.299	0.299	17.43	-0.57	0.57	-0.032	0.032	32.1	14.1	14.1	0.783	0.783
29	22.0	63.5	41.5	41.5	1.886	1.886	24.089	2.089	2.089	0.095	0.095	24.053	2.053	2.053	0.093	0.093	24.01	2.01	2.01	0.091	0.091	26.9	4.9	4.9	0.223	0.223
30	25.4	30.4	5.0	5.0	0.197	0.197	23.412	-1.988	1.988	-0.078	0.078	23.062	-2.338	2.338	-0.092	0.092	28.99	3.59	3.59	0.141	0.141	29.0	3.6	3.6	0.142	0.142
31	21.1	21.7	0.6	0.6	0.028	0.028	17.247	-3.853	3.853	-0.183	0.183	17.247	-3.853	3.853	-0.183	0.183	19.77	-1.33	1.33	-0.063	0.063	20.0	-1.1	1.1	-0.052	0.052
32	21.8	29.9	8.1	8.1	0.372	0.372	20.340	-1.460	1.460	-0.067	0.067	20.504	-1.296	1.296	-0.059	0.059	22.59	0.79	0.79	0.036	0.036	24.0	2.2	2.2	0.101	0.101
33	34.6	37.8	3.2	3.2	0.092	0.092	31.231	-3.369	3.369	-0.097	0.097	31.231	-3.369	3.369	-0.097	0.097	35.12	0.52	0.52	0.015	0.015	39.6	5.0	5.0	0.145	0.145
34	31.4	38.6	7.2	7.2	0.229	0.229	29.083	-2.317	2.317	-0.074	0.074	29.083	-2.317	2.317	-0.074	0.074	31.94	0.54	0.54	0.017	0.017	31.1	-0.3	0.3	-0.010	0.010
35	22.7	28.7	6.0	6.0	0.264	0.264	22.016	-0.684	0.684	-0.030	0.030	21.830	-0.870	0.870	-0.038	0.038	21.94	-0.76	0.76	-0.033	0.033	23.4	0.7	0.7	0.031	0.031
36	27.8	32.1	4.3	4.3	0.155	0.155	22.151	-5.649	5.649	-0.203	0.203	22.151	-5.649	5.649	-0.203	0.203	24.52	-3.28	3.28	-0.118	0.118	25.6	-2.2	2.2	-0.079	0.079
37	21.6	80.7	59.1	59.1	2.736	2.736	22.337	0.737	0.737	0.034	0.034	22.337	0.737	0.737	0.034	0.034	17.64	-3.96	3.96	-0.183	0.183	24.3	2.7	2.7	0.125	0.125
38	32.4	32.6	0.2	0.2	0.006	0.006	28.764	-3.636	3.636	-0.112	0.112	28.764	-3.636	3.636	-0.111	0.112	32.62	0.22	0.22	0.007	0.007	41.1	8.7	8.7	0.269	0.269
39	27.0	48.2	21.2	21.2	0.785	0.785	16.449	-10.551	10.551	-0.391	0.391	16.449	-10.551	10.551	-0.391	0.391	28.98	1.98	1.98	0.073	0.073	26.7	-0.3	0.3	-0.011	0.011
40	35.9	48.8	12.9	12.9	0.389	0.389	30.159	-5.741	5.741	-0.160	0.160	30.018	-5.882	5.882	-0.164	0.164	36.62	0.72	0.72	0.020	0.020	35.2	-0.7	0.7	-0.019	0.019
41	28.4	49.7	21.3	21.3	0.750	0.750	26.761	-1.639	1.639	-0.058	0.058	26.761	-1.639	1.639	-0.058	0.058	29.19	0.79	0.79	0.028	0.028	32.7	4.3	4.3	0.151	0.151
42	24.1	81.7	57.6	57.6	2.390	2.390	21.092	-3.008	3.008	-0.125	0.125	21.092	-3.008	3.008	-0.125	0.125	22.95	-1.15	1.15	-0.048	0.048	34.8	10.7	10.7	0.444	0.444
43	24.9	81.8	56.9	56.9	2.285	2.285	22.964	-1.936	1.936	-0.078	0.078	23.967	-0.933	0.933	-0.037	0.037	23.76	-1.14	1.14	-0.046	0.046	27.7	2.8	2.8	0.112	0.112
44	16.2	98.9	82.7	82.7	5.105	5.105	18.135	1.935	1.935	0.119	0.119	18.058	1.858	1.858	0.115	0.115	26.95	10.75	10.75	0.664	0.664	32.2	16.0	16.0	0.988	0.988
45	23.6	80.6	57.0	57.0	2.415	2.415	24.464	0.864	0.864	0.037	0.037	24.291	0.691	0.691	0.029	0.029	16.62	-6.98	6.98	-0.296	0.296	45.8	22.2	22.2	0.941	0.941
46	30.3	74.8	44.5	44.5	1.469	1.469	26.533	-3.767	3.767	-0.124	0.124	27.364	-2.936	2.936	-0.097	0.097	28.34	-1.96	1.96	-0.065	0.065	49.5	19.2	19.2	0.634	0.634
47	32.5	67.0	34.5	34.5	1.062	1.062	25.304	-7.196	7.196	-0.221	0.221	24.027	-8.473	8.473	-0.261	0.261	29.76	-2.74	2.74	-0.084	0.084	24.2	-8.3	8.3	-0.255	0.255
48	21.1	86.3	65.2	65.2	3.090	3.090	23.996	2.896	2.896	0.137	0.137	29.098	7.998	7.998	0.379	0.379	31.97	10.87	10.87	0.515	0.515	56.8	35.7	35.7	1.692	1.692
49	27.9	35.4	7.5	7.5	0.269	0.269	29.337	1.437	1.437	0.051	0.051	29.337	1.437	1.437	0.051	0.051	27.64	-0.26	0.26	-0.009	0.009	32.6	4.7	4.7	0.168	0.168
50	25.1	37.8	12.7	12.7	0.506	0.506	25.197	0.097	0.097	0.004	0.004	25.197	0.097	0.097	0.004	0.004	26.95	1.85	1.85	0.074	0.074	26.1	1.0	1.0	0.040	0.040
51	28.3	33.6	5.3	5.3	0.187	0.187	25.696	-2.604	2.604	-0.092	0.092	25.696	-2.604	2.604	-0.092	0.092	23.63	-4.67	4.67	-0.165	0.165	32.0	3.7	3.7	0.131	0.131
min	16.20	21.70	-4.0	0.100	-0.120	0.003	16.449	-10.551	0.097	-0.391	0.004	16.449	-10.551	0.097	-0.391	0.004	14.490	-6.980	0.220	-0.296	0.007	20.000	-8.300	0.100	-0.255	0.003
max	43.20	98.90	82.7	82.700	5.105	5.105	36.564	5.230	10.551	0.291	0.391	36.564	7.998	10.551	0.379	0.391	40.320	10.870	10.870	0.664	0.664	56.800	35.700	35.700	1.692	1.692
mean	27.66	47.76	20.1	20.292	0.886	0.891	25.084	-2.576	3.484	-0.079	0.124	25.203	-2.457	3.883	-0.073	0.129	26.858	-0.802	2.255	-0.021	0.090	31.217	3.558	5.365	0.169	0.226

Table 17
Endothelial cell pleomorphism (HEX) results (per cent [%] values) and associated errors

										Endothelial cell pleomorphism (HEX) results (in per cent [%] values) and associated errors																	
Img	Manual	NAVIS	Δx_1	$\lvert\Delta x_1\rvert$	δ_{x1}	$\lvert\delta_{x1}\rvert$	Prop(T1)	Δx_2	$\lvert\Delta x_2\rvert$	δ_{x2}	$\lvert\delta_{x2}\rvert$	Prop(T2)	Δx_3	$\lvert\Delta x_3\rvert$	δ_{x3}	$\lvert\delta_{x3}\rvert$	JPVG etal	Δx_4	$\lvert\Delta x_4\rvert$	δ_{x4}	$\lvert\delta_{x4}\rvert$	Selig etal	Δx_5	$\lvert\Delta x_5\rvert$	δ_{x5}	$\lvert\delta_{x5}\rvert$
0	56.9	56.5	-0.4	0.4	-0.007	0.007	57.895	0.995	0.995	0.017	0.017	57.895	0.995	0.995	0.017	0.017	50.00	-6.90	6.90	-1.213e-01	1.213e-01	52.3	-4.6	4.6	-0.081	0.081
1	66.2	50.0	-16.2	16.2	-0.245	0.245	65.385	-0.815	0.815	-0.012	0.012	65.385	-0.815	0.815	-0.012	0.012	68.42	2.22	2.22	3.353e-02	3.353e-02	55.2	-11.0	11.0	-0.166	0.166
2	40.4	43.1	2.7	2.7	0.067	0.067	43.243	2.843	2.843	0.070	0.070	43.243	2.843	2.843	0.070	0.070	52.00	11.60	11.60	2.871e-01	2.871e-01	30.2	-10.2	10.2	-0.252	0.252
3	44.7	36.5	-8.2	8.2	-0.183	0.183	42.254	-2.446	2.446	-0.055	0.055	42.254	-2.446	2.446	-0.055	0.055	46.15	1.45	1.45	3.244e-02	3.244e-02	41.1	-3.6	3.6	-0.081	0.081
4	57.7	57.0	-0.7	0.7	-0.012	0.012	55.556	-2.144	2.144	-0.037	0.037	55.556	-2.144	2.144	-0.037	0.037	62.79	5.09	5.09	8.821e-02	8.821e-02	58.1	0.4	0.4	0.007	0.007
5	62.6	64.0	1.4	1.4	0.022	0.022	57.971	-4.629	4.629	-0.074	0.074	57.971	-4.629	4.629	-0.074	0.074	62.96	0.36	0.36	5.751e-03	5.751e-03	54.3	-8.3	8.3	-0.133	0.133
6	41.2	36.4	-4.8	4.8	-0.117	0.117	39.474	-1.726	1.726	-0.042	0.042	39.474	-1.726	1.726	-0.042	0.042	40.74	-0.46	0.46	-1.117e-02	1.117e-02	40.2	-1.0	1.0	-0.024	0.024
7	59.3	22.5	-36.8	36.8	-0.621	0.621	53.061	-6.239	6.239	-0.105	0.105	53.061	-6.239	6.239	-0.105	0.105	53.85	-5.45	5.45	-9.191e-02	9.191e-02	40.4	-18.9	18.9	-0.319	0.319
8	69.8	35.7	-34.1	34.1	-0.489	0.489	48.571	-21.229	21.229	-0.304	0.304	48.571	-21.229	21.229	-0.304	0.304	87.10	17.30	17.30	2.479e-01	2.479e-01	62.1	-7.7	7.7	-0.110	0.110
9	58.5	29.5	-29.0	29.0	-0.496	0.496	52.174	-6.326	6.326	-0.108	0.108	52.174	-6.326	6.326	-0.108	0.108	50.00	-8.50	8.50	-1.453e-01	1.453e-01	64.7	6.2	6.2	0.106	0.106
10	62.7	44.2	-18.5	18.5	-0.295	0.295	54.412	-8.288	8.288	-0.132	0.132	54.286	-8.414	8.414	-0.134	0.134	62.75	0.05	0.05	7.974e-04	7.974e-04	52.3	-10.4	10.4	-0.166	0.166
11	53.8	34.2	-19.6	19.6	-0.364	0.364	62.857	9.057	9.057	0.168	0.168	62.857	9.057	9.057	0.168	0.168	66.67	12.87	12.87	2.392e-01	2.392e-01	42.6	-11.2	11.2	-0.208	0.208
12	45.5	39.5	-6.0	6.0	-0.132	0.132	31.707	-13.793	13.793	-0.303	0.303	30.120	-15.380	15.380	-0.338	0.338	47.95	2.45	2.45	5.385e-02	5.385e-02	43.0	-2.5	2.5	-0.055	0.055
13	52.4	49.5	-2.9	2.9	-0.055	0.055	45.000	-7.400	7.400	-0.141	0.141	45.000	-7.400	7.400	-0.141	0.141	45.28	-7.12	7.12	-1.359e-01	1.359e-01	49.4	-3.0	3.0	-0.057	0.057
14	40.6	33.3	-7.3	7.3	-0.180	0.180	41.071	0.471	0.471	0.012	0.012	41.071	0.471	0.471	0.012	0.012	34.29	-6.31	6.31	-1.554e-01	1.554e-01	41.2	0.6	0.6	0.015	0.015
15	54.1	51.3	-2.8	2.8	-0.052	0.052	53.846	-0.254	0.254	-0.005	0.005	52.308	-1.792	1.792	-0.033	0.033	43.18	-10.92	10.92	-2.018e-01	2.018e-01	46.5	-7.6	7.6	-0.140	0.140
16	50.0	45.5	-4.5	4.5	-0.090	0.090	48.214	-1.786	1.786	-0.036	0.036	48.214	-1.786	1.786	-0.036	0.036	44.19	-5.81	5.81	-1.162e-01	1.162e-01	39.0	-11.0	11.0	-0.220	0.220
17	57.7	55.0	-2.7	2.7	-0.047	0.047	52.632	-5.068	5.068	-0.088	0.088	53.535	-4.165	4.165	-0.072	0.072	54.05	-3.65	3.65	-6.326e-02	6.326e-02	56.8	-0.9	0.9	-0.016	0.016
18	44.8	42.1	-2.7	2.7	-0.060	0.060	47.826	3.026	3.026	0.068	0.068	46.667	1.867	1.867	0.042	0.042	46.67	1.87	1.87	4.174e-02	4.174e-02	42.6	-2.2	2.2	-0.049	0.049
19	48.8	55.6	6.8	6.8	0.139	0.139	43.548	-5.252	5.252	-0.108	0.108	43.548	-5.252	5.252	-0.108	0.108	47.83	-0.97	0.97	-1.988e-02	1.988e-02	43.0	-5.8	5.8	-0.119	0.119
20	57.5	52.3	-5.2	5.2	-0.090	0.090	44.643	-12.857	12.857	-0.224	0.224	40.351	-17.149	17.149	-0.298	0.298	55.26	-2.24	2.24	-3.896e-02	3.896e-02	41.6	-15.9	15.9	-0.277	0.277
21	60.9	31.7	-29.2	29.2	-0.479	0.479	66.038	5.138	5.138	0.084	0.084	66.038	5.138	5.138	0.084	0.084	57.58	-3.32	3.32	-5.452e-02	5.452e-02	58.1	-2.8	2.8	-0.046	0.046
22	52.6	48.7	-3.9	3.9	-0.074	0.074	47.826	-4.774	4.774	-0.091	0.091	47.826	-4.774	4.774	-0.091	0.091	48.78	-3.82	3.82	-7.262e-02	7.262e-02	46.8	-5.8	5.8	-0.110	0.110
23	45.1	45.7	0.6	0.6	0.013	0.013	43.662	-1.438	1.438	-0.032	0.032	43.662	-1.438	1.438	-0.032	0.032	47.92	2.82	2.82	6.253e-02	6.253e-02	40.8	-4.3	4.3	-0.095	0.095
24	52.2	52.0	-0.2	0.2	-0.004	0.004	50.000	-2.200	2.200	-0.042	0.042	50.000	-2.200	2.200	-0.042	0.042	55.56	3.36	3.36	6.437e-02	6.437e-02	54.0	1.8	1.8	0.034	0.034
25	66.7	34.7	-32.0	32.0	-0.480	0.480	52.632	-14.068	14.068	-0.211	0.211	52.632	-14.068	14.068	-0.211	0.211	69.23	2.63	2.63	3.793e-02	3.793e-02	63.2	-3.5	3.5	-0.052	0.052
26	43.9	35.8	-8.1	8.1	-0.185	0.185	46.939	3.039	3.039	0.069	0.069	46.939	3.039	3.039	0.069	0.069	46.43	2.63	2.63	5.763e-02	5.763e-02	53.3	9.4	9.4	0.214	0.214
27	73.4	64.2	-9.2	9.2	-0.125	0.125	61.017	-12.383	12.383	-0.169	0.169	61.017	-12.383	12.383	-0.169	0.169	80.00	6.60	6.60	8.992e-02	8.992e-02	61.9	-11.5	11.5	-0.157	0.157
28	59.5	23.4	-36.1	36.1	-0.607	0.607	42.424	-17.076	17.076	-0.287	0.287	45.455	-14.045	14.045	-0.236	0.236	55.00	-4.50	4.50	-7.563e-02	7.563e-02	50.0	-9.5	9.5	-0.160	0.160
29	56.4	21.7	-34.7	34.7	-0.615	0.615	47.500	-8.900	8.900	-0.158	0.158	47.500	-8.900	8.900	-0.158	0.158	69.23	12.83	12.83	2.275e-01	2.275e-01	38.5	-17.9	17.9	-0.317	0.317
30	54.0	50.7	-3.3	3.3	-0.061	0.061	50.000	-4.000	4.000	-0.074	0.074	49.057	-4.943	4.943	-0.092	0.092	58.33	4.33	4.33	8.019e-02	8.019e-02	51.6	-2.4	2.4	-0.044	0.044
31	61.4	65.7	4.3	4.3	0.070	0.070	64.516	3.116	3.116	0.051	0.051	64.516	3.116	3.116	0.051	0.051	55.26	-6.14	6.14	-1.000e-01	1.000e-01	61.5	0.1	0.1	0.002	0.002
32	55.8	56.3	0.5	0.5	0.009	0.009	43.056	-12.744	12.744	-0.228	0.228	42.466	-13.334	13.334	-0.239	0.239	50.85	-4.95	4.95	-8.871e-02	8.871e-02	57.0	1.2	1.2	0.022	0.022
33	59.2	46.2	-13.0	13.0	-0.220	0.220	35.938	-23.263	23.263	-0.393	0.393	35.938	-23.263	23.263	-0.393	0.393	61.54	2.34	2.34	3.953e-02	3.953e-02	37.2	-22.0	22.0	-0.372	0.372
34	59.8	56.3	-3.5	3.5	-0.059	0.059	60.000	0.200	0.200	0.003	0.003	60.000	0.200	0.200	0.003	0.003	54.69	-5.11	5.11	-8.548e-02	8.548e-02	56.0	-3.8	3.8	-0.064	0.064
35	55.8	57.3	1.5	1.5	0.027	0.027	45.977	-9.823	9.823	-0.176	0.176	48.315	-7.485	7.485	-0.134	0.134	57.38	1.58	1.58	2.832e-02	2.832e-02	53.4	-2.4	2.4	-0.043	0.043
36	56.8	54.4	-2.4	2.4	-0.042	0.042	50.000	-6.800	6.800	-0.120	0.120	50.000	-6.800	6.800	-0.120	0.120	47.83	-8.97	8.97	-1.579e-01	1.579e-01	53.0	-3.8	3.8	-0.067	0.067
37	64.7	27.6	-37.1	37.1	-0.573	0.573	47.727	-16.973	16.973	-0.262	0.262	47.727	-16.973	16.973	-0.262	0.262	82.61	17.91	17.91	2.768e-01	2.768e-01	67.4	2.7	2.7	0.042	0.042
38	56.8	50.0	-6.8	6.8	-0.120	0.120	44.444	-12.356	12.356	-0.218	0.218	44.444	-12.356	12.356	-0.218	0.218	56.41	-0.39	0.39	-6.866e-03	6.866e-03	48.6	-8.2	8.2	-0.144	0.144
39	58.3	37.3	-21.0	21.0	-0.360	0.360	40.541	-17.759	17.759	-0.305	0.305	40.541	-17.759	17.759	-0.305	0.305	56.52	-1.78	1.78	-3.053e-02	3.053e-02	51.2	-7.1	7.1	-0.122	0.122
40	51.4	47.9	-3.5	3.5	-0.068	0.068	36.585	-14.815	14.815	-0.288	0.288	36.585	-14.815	14.815	-0.288	0.288	51.43	0.03	0.03	5.837e-04	5.837e-04	46.6	-4.8	4.8	-0.093	0.093
41	52.4	28.1	-24.3	24.3	-0.464	0.464	44.444	-7.956	7.956	-0.152	0.152	44.444	-7.956	7.956	-0.152	0.152	53.33	0.93	0.93	1.775e-02	1.775e-02	41.2	-11.2	11.2	-0.214	0.214
42	62.3	30.3	-32.0	32.0	-0.514	0.514	45.238	-17.062	17.062	-0.274	0.274	45.238	-17.062	17.062	-0.274	0.274	60.00	-2.30	2.30	-3.692e-02	3.692e-02	51.9	-10.4	10.4	-0.167	0.167
43	48.5	22.2	-26.3	26.3	-0.542	0.542	66.667	18.167	18.167	0.375	0.375	50.000	1.500	1.500	0.031	0.031	63.64	15.14	15.14	3.122e-01	3.122e-01	40.0	-8.5	8.5	-0.175	0.175
44	63.4	26.9	-36.5	36.5	-0.576	0.576	35.000	-28.400	28.400	-0.448	0.448	40.000	-23.400	23.400	-0.369	0.369	50.00	-13.40	13.40	-2.114e-01	2.114e-01	42.1	-21.3	21.3	-0.336	0.336
45	60.0	30.8	-29.2	29.2	-0.487	0.487	47.059	-12.941	12.941	-0.216	0.216	50.000	-10.000	10.000	-0.167	0.167	69.23	9.23	9.23	1.538e-01	1.538e-01	39.5	-20.5	20.5	-0.342	0.342
46	43.6	29.0	-14.6	14.6	-0.335	0.335	20.690	-22.910	22.910	-0.525	0.525	21.429	-22.171	22.171	-0.509	0.509	25.00	-18.60	18.60	-4.266e-01	4.266e-01	21.3	-22.3	22.3	-0.511	0.511
47	55.0	28.7	-26.3	26.3	-0.478	0.478	42.105	-12.895	12.895	-0.234	0.234	50.000	-5.000	5.000	-0.091	0.091	62.50	7.50	7.50	1.364e-01	1.364e-01	50.0	-5.0	5.0	-0.091	0.091
48	40.9	29.4	-11.5	11.5	-0.281	0.281	30.435	-10.465	10.465	-0.256	0.256	31.818	-9.082	9.082	-0.222	0.222	22.22	-18.68	18.68	-4.567e-01	4.567e-01	23.8	-17.1	17.1	-0.418	0.418
49	55.3	43.0	-12.3	12.3	-0.222	0.222	47.826	-7.474	7.474	-0.135	0.135	50.000	-5.300	5.300	-0.096	0.096	58.54	3.24	3.24	5.859e-02	5.859e-02	39.2	-16.1	16.1	-0.291	0.291
50	52.3	39.0	-13.3	13.3	-0.254	0.254	28.571	-23.729	23.729	-0.454	0.454	28.571	-23.729	23.729	-0.454	0.454	54.55	2.25	2.25	4.302e-02	4.302e-02	51.5	-0.8	0.8	-0.015	0.015
51	62.0	55.2	-6.8	6.8	-0.110	0.110	58.333	-3.667	3.667	-0.059	0.059	58.333	-3.667	3.667	-0.059	0.059	61.36	-0.64	0.64	-1.032e-02	1.032e-02	53.6	-8.4	8.4	-0.135	0.135
min	40.400	21.700	-37.100	0.20	-0.621	0.004	20.690	-28.400	0.200	-0.525	0.003	21.429	-23.729	0.200	-0.509	0.003	22.220	-18.68	0.030	-4.567e-01	5.837e-04	21.300	-22.300	0.100	-0.511	0.002
max	73.400	65.700	6.800	37.10	0.139	0.621	66.667	18.167	28.400	0.375	0.525	66.038	9.057	23.729	0.168	0.509	87.100	17.91	18.680	3.122e-01	4.567e-01	67.400	9.400	22.300	0.214	0.511
mean	55.108	42.383	-12.725	13.41	-0.222	0.235	47.779	-7.328	9.100	-0.128	0.163	47.770	-7.338	8.423	-0.129	0.150	55.098	-0.01	5.795	-3.802e-03	1.083e-01	48.092	-7.015	7.877	-0.127	0.144

Segmentation of endothelial cells of the cornea from the distance map of confocal microscope images

Raidel Herrera-Pereda, Alberto Taboada Crispi, Danilo Babin, Wilfried Philips

- A difference of Gaussian is applied to enhance cell borders and to obtain the inter-cellular space with minimal value, which we then used as a threshold for obtaining a binary image.
- A frequency-domain analysis allows obtaining a global adaptive threshold value per image for automatically removing artifacts in the binary images.
- Local maxima, selected in the distance map of the binary image, are used as centers of circles inscribed in the cells. A selection of the inscribed circles is intended to detect individual cells, aiming also to separate those cells that appear merged in the image.
- The segmentation of the cell's contours is achieved simply by labeling each background pixel according to its distance to the nearest foreground object.
- Quantification and comparison with ground truth and two methods are achieved for measuring clinical parameters of interest and assessing the results, including cell count, cell density, polymegathism, and pleomorphism. Results outperform those from one of the methods in all quantified parameters and surpass another method in estimated polymegathism.

Declaration of interests

☐X The authors declare that they have no known competing financial interests or personal relationships that could have appeared to influence the work reported in this paper.

☐The authors declare the following financial interests/personal relationships which may be considered as potential competing interests: